UNIVERSITY OF CALIFORNIA
SANTA CRUZ

ESTIMATING A LOCAL SOURCE APPROXIMATION FOR THE ULTRAVIOLET BACKGROUND RADIATION IN COSMOLOGICAL SETTINGS USING LAMBDA ITERATION

A thesis submitted in partial satisfaction
of the requirements for the degree of

MASTER OF SCIENCE

in

SCIENTIFIC COMPUTING AND APPLIED MATHEMATICS

by

Tayler Quist

September 2020

The Thesis of Tayler Quist
is approved:

Professor Nicholas Brummell

Professor Brant Robertson

Professor Dongwook Lee

Quentin Williams
Acting Vice Provost and Dean of Graduate Studies

Contents

List of Figures

List of Tables

Abstract

Estimating a local source approximation for the ultraviolet background radiation in cosmological settings using Lambda Iteration

by

Tayler Quist

After the epoch of reionization, Lyman continuum radiation permeate the universe. Immediately after reionization (redshifts $z \approx 3-7$), the influence of the cosmic Ultraviolet (UV) background on the Intergalactic Medium (IGM) and the Circumgalactic Medium (CGM) is important to understand. We focus on building a 1D radiative transfer algorithm using the Accelerated Lambda Iteration scheme and the Lambda Iteration scheme to solve the time-independent radiative transfer equation. This approach captures the dynamics of radiation fields, and the convergence, accuracy, and mathematical limitations of these schemes are thoroughly tested. We then expand the algorithm to include a 4th order Runge-Kutta scheme to trace the fraction of Hydrogen atoms between the UV background and the center of a massive galaxy. In our calculations, the UV background dominates the ionization of the IGM and CGM near our example star-forming galaxy.

Dedication and Acknowledgements

This thesis is dedicated in part to my Dad. He has been my only caretaker for over half of my life. He gave me complete freedom to chase my dreams wherever they lead me. I would also like to dedicate this thesis to Dr. Brant Robertson. I was previously discouraged from joining a graduate program because I ”wouldn’t be good enough”. On top of that I couldn’t afford to move halfway across the US to join a graduate program, but Brant made it possible by taking a chance on me as a researcher. Brant helped me gain confidence as a student which allowed me to succeed in grad school. Brant’s support, knowledge, and kindness changed my life for the better. Thank you.

1 Introduction

When dealing with the fluid dynamics of extragalactic systems, the fluxes of energy and momentum carried by the radiation field can be significant or, depending on scale, dominant [1]. It is important to implement radiation hydrodynamics (RHD) instead of pure hydrodynamics in regions where the local dynamics are radiation dominated or where radiation contributes significantly to the dynamics. In this thesis we specifically focus on the early, matter dominated universe just after the epoch of reionization. Cosmic reionization refers to the ionization of the neutral intergalactic medium (NIM). The NIM referred to here is the combination of Hydrogen and Helium distributed across the universe. In the very early universe, small fluctuations in matter density caused certain regions to collapse and form the first stars and galaxies (i.e. luminous sources). According to sources from Rosdahl & Teyssier 2015 [2] radiation hydrodynamics are important in the feedback from supernovae and AGN. The uneven distribution of gas also corresponded to the creation of ”radiation sinks” where the gas density is thick enough to absorb the radiation and prevent further propagation [3]. Prominent radiation sinks include cold gas and dust found in objects like nebulae. When these feedback mechanisms are modeled via pure hydrodynamics there can be a disconnect between cosmological simulation results and observations. For example simulations that have modeled the influence of radiation solved from “first principles” using RHD have been capable of conquering a number of problems including the overcooling issue that causes over-compact galaxies which are inconsistent with observations [2].

It is important to point out that stars and galaxies are not the only notable sources of radiation in the young universe. Today we detect a microwave signal that is almost uniform from every direction, commonly known as the Cosmic Microwave Background (CMB) [4] [5]. Although scientists detect this signal as a microwave frequency to-

day, the frequency of the CMB has not been constant throughout time [6]. There are other radiation backgrounds, and during the epoch of reionization and shortly after the epoch (between a redshift of $z = 3$ and $z = 7$) the ultraviolet light (UV) from star forming galaxies provided a source or large-scale heating for the NIM [7]. Since the UV background is a large-scale source in the era of interest it is included in our main test experiment.

There have been a variety of numerical models that have used RHD to model the era of interest [8] [9] [10] [11] [12] [13]. We aim to develop an initial 1D radiative transfer model that, in the future, can be extended to a full 2D and 3D algorithm that couples to the 3D hydrodynamics produced by the parallelized, cosmological code Cholla [14].

The goal of this thesis is to produce a code that uses a higher order approximation to solve the equation of radiative transfer for 1D problems and 2D and 3D problems with spatially symmetric properties. We then use this code to study how the variations in brightness of the UV background affect the ionization of Hydrogen gas between a massive galaxy and the UV background. This allows us to gather further insight about the period after the epoch of reionization.

We start this thesis off by introducing the radiative transfer equation and other relevant equations in Section 2. We then discuss details about the numerical methods used in the code including the Accelerated Lambda Iteration scheme (ALI), the Lambda Iteration scheme (LI), a 4th order Runge-Kutta solver, and the method of Short Characteristics in Section 3. We then perform a series of test calculations used to check the accuracy and convergence of the code in Section 4. Section 5 discusses the details and setup of the cosmological experiment. The results of this experiment are presented in Section 6. Finally Section 7 wraps up our study with a conclusion and summary of the main take-away points.

2 Mathematical Formalism

2.1 The Formal Radiative Transfer Equation

The formal RT equation captures the mathematical and physical understanding of the spatial and time-sensitive variables contributing to changes in the specific intensity. The specific intensity is a frequency dependent brightness that is affected by objects that emit or absorb radiation (photons). This derivation is guided by the method found in Section 2.1 of Petkova & Springel 2009 [15].

We must consider the photon distribution function (PDF) (F_ν) which is a variable that depends on time (t), the spatial coordinate (x), and the photon momentum ($\mathbf{p}$) for a specific frequency or frequency bin (ν). The momentum of a photon is given by the following equation.

$$\mathbf{p} = \frac{h\nu}{c} a(t)\hat{\mathbf{n}} \tag{1}$$

Where h is the Planck constant, $\hat{\mathbf{n}}$ is the direction in which the photon is propagating (which still varies in 1D), and $a(t)$ is the time-dependent cosmological scale factor. This scale factor accounts for the accelerating expansion of the universe that directly decreases the energy of a photon due to the elongation of its wavelength.

In order to have a conservative and differentiable system we must enforce that the PDF remain unaltered along the trajectories of the system [16] [17]. Thus by Liouville's theorem the following equation describes the phase-space continuity relation for the PDF.

$$\frac{\partial F_\nu}{\partial t} + \frac{\partial(\dot{x}F_\nu)}{\partial x} + \frac{\partial(\dot{\mathbf{p}}F_\nu)}{\partial \mathbf{p}} = (emission\ -\ absorption) \tag{2}$$

The *emission* and *absorption* terms represent the photon emission and absorption processes.

Taking the photon distribution function (equation 1) and integrating it with respect to

all possible momenta and spatial directions determines the total number of photons at a given time in the section of interest within the universe (N_ν).

$$N_\nu = \int F_\nu(t,x,\mathbf{p}) d\mathbf{x} d\mathbf{p} \tag{3}$$

This PDF is also used to determine the specific intensity I_ν. Before defining the relation between I_ν and F_ν, we must mathematically define the specific intensity. The specific intensity can be used to define the energy of a photon per frequency interval $d\nu$, in the area dA, over the angle $d\Omega$, in time interval dt [18].

$$dE_\nu = I_\nu d\nu d\Omega dA dt \tag{4}$$

I_ν has units of (erg cm^{-2} s^{-1} Hz^{-1} rad^{-2}). Using the energy equation (equation 4) we can relate F_ν to I_ν by noting that $d^3p = p^2\ dp\ d\Omega$ and $d^3x = c\ dt\ dA$ and integrate with respect to momentum and distance (the 1D spatial dimension) with respect to frequency, solid angle, area, and time [15] [18].

$$I_\nu = h\nu F_\nu \frac{d^3x d^3p}{d\nu d\Omega dA dt} = \frac{h^4\nu^3}{c^2} F_\nu \tag{5}$$

Rearranging the specific intensity definition (equation 5) to solve for F_ν and then plugging it into the conservation equation (equation 2) results in the full RT equation.

$$\frac{1}{c}\frac{\partial I_\nu}{\partial t} + \frac{\mathbf{n}}{a}\frac{\partial I_\nu}{\partial x} - \frac{H}{c}\left(\nu\frac{\partial I_\nu}{\partial \nu} - 3I_\nu\right) = j_\nu - \kappa_\nu I_\nu \tag{6}$$

Where $\mathbf{n}$ is a unit direction vector, κ_ν is the absorption coefficient (cm^2 g^{-1}), and j_ν is the spontaneous emission coefficient (known as the emissivity) (erg cm^{-3} s^{-1} Hz^{-1} rad^{-2}). c is the speed of light (cm s^{-1}), $H = \frac{\dot{a}}{a}$ is the Hubble expansion rate, and $\dot{a}$ is

the time derivative of the cosmological scale factor.

Note that the 3D version of equation 6 has three spatial variables, a time variable, a frequency variable, and directional angles. This poses a computational barrier in terms of setting up a mesh grid and is even computationally limiting when dealing with the 1D case. Therefore moment-based approximations are used to simplify the problem for cosmological simulations [15]. For this study we used the non-dimensional, time-independent transfer equation to solve for the specific intensity [1]. Where α_ν is the extinction coefficient (i.e. the opacity) (cm^{-1}) which depends on the absorption coefficient (the mass-weighted opacity) and particle density (cm^{-3}). S_ν is the source function with the same units as the specific intensity (erg cm^{-2} s^{-1} Hz^{-1} rad^{-2}). We dive into the numerical details of the source function in Section 2.2.

$$\frac{\partial I_\nu}{\partial x} = \alpha_\nu(S_\nu(x) - I_\nu(\mathbf{x})) \tag{7}$$

Since we numerically approximate the solution to equation 7 within each iteration of the algorithm (numerical details in Section 3) the other variables that depend on the specific intensity also needed to be updated each iteration. This translates to updating two specific intensity values per grid cell per iteration due to the two sources. Since the propagation of radiation is different for the galaxy and the UV background we must calculate them separately. However there can only be one source function representing the environment that takes into account both specific intensity values at each grid point. Thus we use the average specific intensity value. The mean specific intensity is formally defined for a amount of sources in the following equation.

$$J_\nu = \frac{1}{a}\sum_{k=1}^{a} I_\nu^k \tag{8}$$

This moment-based approximation becomes very simple when using the Eddington approximation [19], which we adopt in our 1D simulations.

In the next subsection we show how the source function and the other variables depend on the average specific intensity and what they physically mean.

2.2 Mean Specific Intensity and Source Function

This section introduces three new variables: the source function (S_ν), the thermal source function (Planck Function) (B_ν), and the photon destruction probability (ε_{nu}).

In the case of local thermodynamic equilibrium (LTE), the source function is identical to the Planck Function. The Planck Function is generally a measurement of the amount of energy present in a thermal radiation field by a particular wavelength (or frequency) per area per steradian [20].

$$B_\nu(T) = \frac{2h\nu^3}{c^2} \frac{1}{e^{\frac{h\nu}{k_B T}} - 1} \tag{9}$$

Where h is the Planck constant with a value of $h = 6.6162e-27$ $(cm^2 g s^{-1})$, c is the speed of light in $\frac{cm}{s}$, k_B is the Boltzmann constant in $\frac{erg}{K}$, and T is the temperature in Kelvin of the object of interest.

When the process of photon scattering is present, the source function will depend on the local thermal emission and the mean intensity. In this case the definition of the Planck Function above does not capture all of the necessary physics to compute the source function.

The photon destruction probability ε_ν is a dimensionless quantity shaped by how prominent the absorption opacity α_ν^{abs} is in comparison with the total opacity [19]. The total opacity considers not only the absorption opacity but also the scattering opacity α_ν^{sc} of

the medium. We can write the photon destruction probability in the following way.

$$\varepsilon_\nu = \frac{\alpha_\nu^{abs}}{\alpha_\nu^{abs} + \alpha_\nu^{sc}} \tag{10}$$

The quantity ε_ν is a fraction whose values are restricted between 0 and 1. If the absorption opacity is large relative to the scattering opacity, then a photon traveling along a random path is most likely be absorbed rather than scattered. This quantity then acts as the quenching mechanism for the propagating radiation. Equation 10 is not the only way to define the photon destruction probability. In Section 3.3 we give an alternative definition based the number of ionized and neutral atoms in the local area, a quantity that is tracked within the simulation.

We have now defined all of the variables that the source function is dependent on. Logically the source function is formulated by taking into account the thermal source function, the brightness (i.e. specific intensity), and the percentage of photons that are getting quenched at a particular radius.

$$S_\nu = \varepsilon_\nu B_\nu + (1 - \varepsilon_\nu) J_\nu \tag{11}$$

For all of our test cases and our main experiment we assume the Planck Function (B_ν) is in local thermodynamic equilibrium thus $B_\nu = 1$.

In the next section we walk through how to approximate an unknown specific intensity value for a massive galaxy in the epoch of interest.

2.3 Specific Intensity Calculation for an Early Galaxy

For the astrophysical experiment (Section 5) we need to calculate the specific intensity value for the center of our galaxy at redshift $z \sim 3$. In this section we walk through the

mathematical steps for the calculation.

First we needed to determine the rate Q_0 at which photons are released from a source. For galaxies, this rate depends on a number of physical factors and the details of these factors are discussed in Section 5.2.1. Our first estimate for the photon production rate is based on the values originated by the code and case studies produced by [21] and [22]. For star forming galaxies they estimated star formation rates to lie between $Q_0 \approx 10^{53}\frac{1}{s} - 10^{53.7}\frac{1}{s}$. In our calculations, we experimented with star formation rates corresponding to slightly smaller values ranging from $Q_0 = 10^{52.6}\frac{1}{s}$ - $10^{53.4}\frac{1}{s}$ as shown in Section 4.1. The photon production rate is used to compute the luminosity in the hydrogen-ionizing spectrum. Luminosity is the rate of energy produced by these photons and is the backbone to defining the specific intensity. We calculated the luminosity by multiplying the photon production rate by the energy of each photon. We are working with neutral Hydrogen and so the ionizing energy is $13.6eV$ (which we converted into erg).

$$Q_0 \cdot E_{photon} = L_{L\alpha} \tag{12}$$

Equation 12 is the luminosity for the Lyman Continuum. We then needed to make it frequency dependent in order to get the specific luminosity (equation 13).

$$\frac{L_{L\alpha}}{\nu_{photon}} = L_{specific} \tag{13}$$

The photon frequency (ν_{photon}) must be within the range of frequencies corresponding to UV light.

In order to convert a specific luminosity into a specific intensity we need the brightness per area per solid angle. In order to compute the area we first compute what the distance across each numerical grid cell is. The grid spans a physical distance of approximately

Variable	Q_0	E_{photon}	x_{cell}	I_{galaxy}
Value	$10^{52.6}$	$2.1787x10^{-11}$	$1.9197x10^{21}$	$2.8x10^{-16}$
Units	$\frac{1}{s}$	erg	cm	$\frac{erg}{s\ Hz\ cm^2\ ster}$

Table 1: List of values and the respective units used in the calculation to determine the specific intensity of the galaxy.

622 kpc. This means that the distance across each cell is dependent on the number of grid points specified by the user. We ran the experiment on a grid containing 1,000 grid points and thus the value is $x_{cell} \approx 0.622\ kpc$. Since we focused on the grid cell centers, rather than the grid points, we only needed to know half of the distance covered by an entire grid cell.

$$\frac{1}{2}x_{cell} = x_{center} \tag{14}$$

We then use this length as a radius to calculate the area of the sphere around the center of the cell.

$$4\pi x_{center}^2 = A \tag{15}$$

We are solely interested in looking at the area per solid angle of this sphere so we must divide by 4π.

$$\frac{A}{4\pi} = A_{ster} \tag{16}$$

Finally we can make the conversion from specific luminosity to specific intensity by dividing the specific luminosity by the area per solid angle.

$$\frac{L_{specific}}{A_{ster}} = I_{galaxy} \tag{17}$$

Table 1 displays all of the quantitative values for equation 12 and equation 14 for a grid resolution of 1000. The next section covers our methodologies for numerically computing the radiation field.

3 Numerical Methods

3.1 Overview of Different Methods

There are a variety of methods used in the large number of numerical RT solvers. In order to choose which method to use we discuss the definition and traits few common methods below.

One numerical scheme uses discrete ordinate methods that encompass ray coupling and cell coupling methods such as the one found in [23]. The ALI and LI schemes mentioned above fall into this category. These schemes have historically been go-to methods and can be constructed to solve multidimensional problems such as with the Multilevel Accelerated Lambda Iteration (MALI) [24]. These schemes involve integrating the time-independent transfer equation at each time step making them more computationally expensive relative to other well-known methods.

Another method utilizes "closure relations" for the RT moment equations. The M1 closure scheme falls into this category [1] [15] [19]. This scheme assigns and integrates a hierarchy of angular moments where the zero order moment is assigned a relation to the second order moment to create a closed set of equations. The integrations and relations are defined within the Variable Eddington Tensor (VET) [1]. However the VET is computed from the formal solution of the time-dependent transfer equation at every time step like the ALI and LI schemes [1].

The final category of interest is the Monte Carlo method. This is a brute-force solver and one example can be presented by [25]. Although this method can stand alone, it can also be used to solve for the VET in place of using a ray tracing method for solving the M1 closure relations mentioned above [19].

We focus on the computational details of the LI and ALI ray tracing scheme. As mentioned above integrating the time-independent transfer equation must be performed at

every step. The method used to perform this numerical integration is up to the modelers' discretion. In the next section we discuss our chosen numerical method.

3.2 The Method of Short Characteristics

Recall that we are working with a linear, ordinary differential equation (equation 7). The general form of this type of equation is seen in equation 18 below.

$$y' = g(x) - p(x)\, y \tag{18}$$

Where $g(x)$ and $p(x)$ are coefficients that depend on the independent variable x. The general solution to this type of ODE can be written as follows.

$$\mu y = \int \mu g(x)\, dx \tag{19}$$

Where μ is the factor of integration and can be written in terms of the coefficient $p(x)$ (equation 20).

$$\mu = e^{\int p(x)\, dx} \tag{20}$$

When applied to radiative transfer, the solution can be approximated by utilizing the Method of Short Characteristics. The Method of Short Characteristics (MSC) approximates a new specific intensity value (at one grid point) by using the neighboring specific intensity values, the optical depth, and the surrounding source term values. We implement this method by following the the work done by Dullemond & Turolla 2000 [26] (D&T00) and Kunasz & Auer 1988 [27] (K&A88). The algorithm presented by D&T00 is similar to Busche & Hillier 2000 [28], and the work of K&A88 is the backbone of DSJ12 [19]. It is valuable to explicitly mention that JSD12 and DSJ12 [1] [19] both use the method of short characteristics for integrating the time-dependent transfer equation

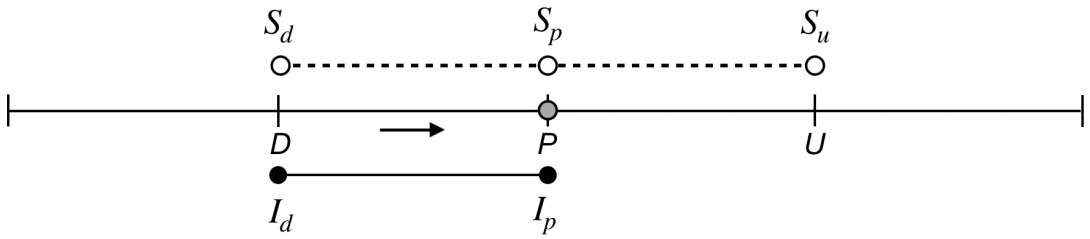

Figure 1: Illustrating where each value comes from when using the MSC in 1D in order to estimate the value of the specific intensity at point P. The arrow denotes the direction the integration (also the direction of the ray).

to compute the VET for RHD applications. This motivated us to choose this method because we want to extend our algorithm to be a full RHD solver in the future.

We will discuss how to solve for the different components of equation 21, which is the MSC numerical solution to equation 7.

$$I_k(P) = e^{-\tau} I_k(D) + S_{interp} \tag{21}$$

The first step is to populate the grid with the respective initial and boundary conditions for the source term, mean intensity, and specific intensity values. We then calculate the interpolated source term from equation 21 by using the neighboring source term values (equation 22). Note that a visualization of how the MSC works can be seen in Figure 1 which displays the virtual grid space used, the location of the source terms, and specific intensity values needed to update the values at point P. Equation 22 defines the full parametric form of the quadratic Bézier interpolation used to calculate the influence of the surrounding source terms on the new specific intensity value.

$$S_{interp} = S_k(D)(1-t)^2 + 2(1-t)t\ S_k(P) + S_k(U)t^2 \tag{22}$$

$S_k(D), S_k(P), S_k(U)$ are the source term values at points D, P, and U respectively as shown in Figure 1. Parameter t defines the interpolation coefficients. For our experiment the source term coefficients solely depend on on the optical depth at points D, P, and U. The three terms in equation 22 are fully defined in equations 24-29. For our particular application, the derivation of these constants is long and tedious but the details can be followed in Olson & Kunasz 1987 [29].

$$S_{interp} = dS_k(D) + pS_k(P) + uS_k(U) \tag{23}$$

$$d = e_0 + \frac{e_2 - (2\Delta\tau + \Delta\tau_{i+1})e_1}{\Delta\tau(\Delta\tau + \Delta\tau_{i+1})} \tag{24}$$

$$p = \frac{(\Delta\tau + \Delta\tau_{i+1})e_1 - e_2}{\Delta\tau\Delta\tau_{i+1}} \tag{25}$$

$$u = \frac{e_2 - \Delta\tau e_1}{\Delta\tau_{i+1}(\Delta\tau + \Delta\tau_{i+1})} \tag{26}$$

$$e_0 = 1 - e^{-\Delta\tau} \tag{27}$$

$$e_1 = \Delta\tau - e_0 \tag{28}$$

$$e_2 = \Delta\tau^2 - 2e_1 \tag{29}$$

In equations 24-29, $\Delta\tau_i$ is the change in optical depth for grid cell i, located between grid points $i - \frac{1}{2}$ (the sequentially previous grid point) and the grid point at $i + \frac{1}{2}$ (which is the current grid point). Note that the $i - \frac{1}{2}$ grid point will be defined by the direction of integration. The quantity $\Delta\tau_{i+1}$ is the change in optical depth between the current grid point $i + \frac{1}{2}$ and the "next" grid point $i + \frac{3}{2}$. Grid point $i + \frac{3}{2}$ will also be defined by the direction of integration. Figure 2 aids in visualizing the labels assigned to each relevant grid point and grid cell for the two possible directions of integration in 1D. We integrate equation 20 in both of these directions for our test experiments and as-

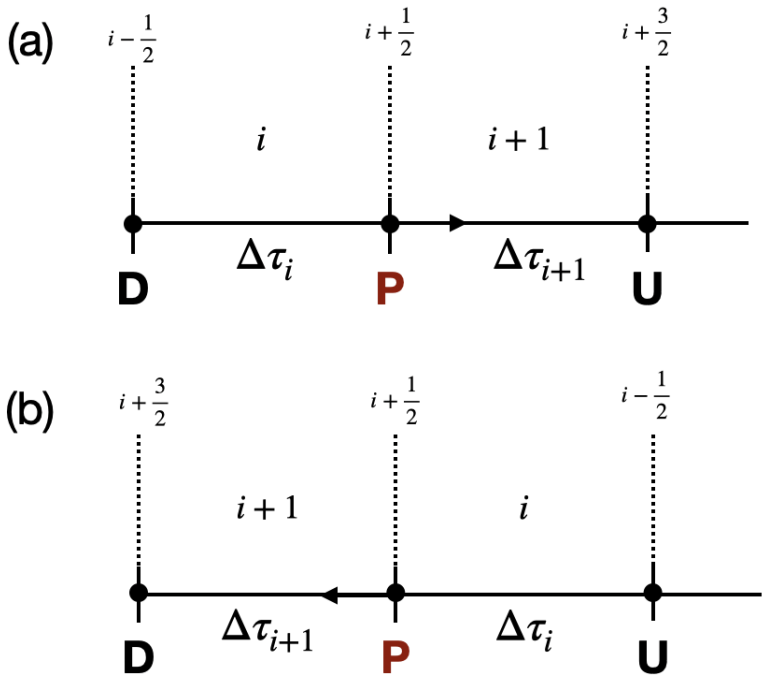

Figure 2: Solving for the solution to the TI transfer equation at point P involves integration from two different directions. The $+$ direction is represented by (a) and the $-$ direction is represented by (b). Grid cell and grid point locations can be represented by i. Any whole integer (eg $i = 0, 1, 2, ...$) represents a grid cell location, while grid points are rational numbers that are a factor of $\frac{1}{2}$ (eg $i = \frac{1}{2}, \frac{3}{2}, ...$). The direction of integration is shown by the arrow and translates to the following rays: (a) I^+ ray (b) $I^-(P)$ ray. The labels D, P, and U are point labels associated with the different coefficients used in the interpolation.

trophysical experiment. Since we are working with two directions, and therefore two rays pointing in each direction, we used the two-stream approximation (Section 4.2) as one of our main test experiments. This experiment is used to verify the accuracy and precision of our algorithm.

Since the coefficients in equations 24-29 differ for each direction of integration, we assign a $+$ and $-$ value to each ray therefore designating the direction of integration respectively. The coefficients corresponding to each $+$ and $-$ ray are listed in equations 30-35. Equations 30-35 can be expanded to a higher number of rays.

$$I^+_{i+\frac{1}{2}} = I^+_{i-\frac{1}{2}}\, e^{-\Delta\tau_{i-1}} + d^+\, S_{i-\frac{1}{2}} + p^+\, S_{i+\frac{1}{2}} + u^+\, S_{i+\frac{3}{2}} \tag{30}$$

$$e^+_0 = 1 - e^{-\Delta\tau_i},\;\; e^+_1 = \Delta\tau_i - e^+_0,\;\; e^+_2 = \Delta\tau_i^2 - 2e^+_1 \tag{31}$$

$$d^+ = e^+_0 + \frac{e^+_2 - (2\Delta\tau_i + \Delta\tau_{i+1})e^+_1}{\Delta\tau_i(\Delta\tau_i + \Delta\tau_{i+1})},\; p^+ = \frac{(\Delta\tau_i + \Delta\tau_{i+1})e^+_1 - e^+_2}{\Delta\tau_i\Delta\tau_{i+1}},\; u^+ = \frac{e^+_2 - \Delta\tau_i e^+_1}{\Delta\tau_{i+1}(\Delta\tau_i + \Delta\tau_{i+1})} \tag{32}$$

$$I^-_{i+\frac{1}{2}} = I^-_{i+\frac{3}{2}}\, e^{-\Delta\tau_{i+1}} + u^-\, S_{i-\frac{1}{2}} + p^-\, S_{i+\frac{1}{2}} + d^-\, S_{i+\frac{3}{2}} \tag{33}$$

$$e^-_0 = 1 - e^{-\Delta\tau_{i+1}},\;\; e^-_1 = \Delta\tau_{i+1} - e^-_0,\;\; e^-_2 = \Delta\tau_{i+1}^2 - 2e^-_1 \tag{34}$$

$$d^- = e^-_0 + \frac{e^-_2 - (2\Delta\tau_i + \Delta\tau_{i+1})e^-_1}{\Delta\tau_{i+1}(\Delta\tau_i + \Delta\tau_{i+1})},\; p^- = \frac{(\Delta\tau_i + \Delta\tau_{i+1})e^-_1 - e^-_2}{\Delta\tau_i\Delta\tau_{i+1}},\; u^- = \frac{e^-_2 - \Delta\tau_{i+1} e^-_1}{\Delta\tau_i(\Delta\tau_i + \Delta\tau_{i+1})} \tag{35}$$

This concludes the discussion of the integration of the time-independent transfer equation that is performed each iteration until convergence is reached. The next section discusses how we utilize the result from the converged iterations of the MSC.

3.3 Hydrogen Ion Fraction and Photon Destruction Probability

The Hydrogen ion fraction ($Q_{H_{II}}$) is the ratio of ionized Hydrogen atoms to the total number of Hydrogen atoms. The Hydrogen ion fraction is a critical quantity when considering the evolution of the specific intensity for a variety of reasons.

Ionized Hydrogen atoms scatter photons and non-ionized atoms absorb photons. Thus tracking $Q_{H_{II}}$ is a different way of measuring the scattering and absorption of photons. This allows us to use $Q_{H_{II}}$ to define the photon destruction probability (i.e. the opacity) rather than using I_ν.

As discussed in Section 3.2, the opacity has the ability to prevent radiation from propagating due to the opacity's dependence on the gas density. Density depends on the temperature of the gas. If the gas is hot it is thinly spread out across a specified space

causing the density to be sparse. Making it harder for photons to interact with the atoms. If the gas is hot enough to be ionized, or if a fraction of the gas is ionized, once again the photons do not interact with these atoms. This happens due to the fact they are not capable of absorbing photons. In either of these cases, photons are able to travel a larger distance, or all the way through the gas. On the contrary, if the gas is cold then the atoms are closer together (more dense) and acted like a net catching and absorbing photons quickly. Very few photons, or none of the photons, are able to penetrate through the entirety of the gas. Therefore $Q_{H_{II}}$ also influences the density of the Hydrogen gas between the two sources which in turn affect the opacity and optical depth across the grid.

$Q_{H_{II}}$ increases or decreases based on the strength of the specific intensity and the density. It evolves based on the linear, constant coefficient, ordinary differential equation listed below [14].

$$\dot{Q}_{H_{II}} = \frac{\dot{n}_{ion}}{\langle n_H \rangle} \frac{Q_{H_{II}}}{t_{rec}} \tag{36}$$

$\dot{n}_{ion}$ is the ionizing photon rate ($\frac{photons}{s}$). $\langle n_H \rangle$ is the hydrogen number density (cm^{-3}). Finally t_{rec} is the intergalactic medium recombination time. Recombination time is the time it takes an ionized nucleus to recombine with an electron. The equations for each of these variables are listed below in equations 37 - 40. $Q_{H_{II}}$ varies from grid cell to grid cell since the gas within the distance covered by one grid cell can be ionized while its neighbor has neutral gas. This is a limit to a computational grid; all of the gas in the grid cell is considered ionized even if physically only a portion of the gas in the grid cell is ionized.

$$\langle n_H \rangle = \rho X_p \tag{37}$$

X_p is the fraction of the gas that is made of Hydrogen which is the same as the fraction of Hydrogen in the Universe at this redshift ($X_p = 0.76$).

$$\dot{n}_{ion} = J_\nu \frac{4\pi\xi_{ion}}{L} \tag{38}$$

$$L = \frac{1}{C_{H_II}(1 - Q_{H_II})\langle n_H \rangle \sigma_\nu} \tag{39}$$

C_{H_II} is the recombination clumping factor for the intergalactic medium at a redshift of $z = 3$ and $T = 20,000K$ [30] and a value of $C_{H_II} = 3$. σ_ν is the photoionization cross section of Hydrogen atoms and has a value of $\sigma_\nu = 7.91x10^{-18}$ cm^2. ξ_{ion} is the ionization photon production efficiency approximated from [21] and [22] to be $\xi_{ion} = 10^{25.25}\ \frac{erg}{Hz}$.

$$t_{rec} = \frac{1}{C_{H_II}\alpha_B(T)(1 + \frac{Y_P}{4X_P})\langle n_H \rangle (1+z)^3} \tag{40}$$

Where $\alpha_B(T)$ is the recombination coefficient with a value of $\alpha_B(T) = 2.6x10^{-16}\ \frac{cm^3}{s}$. Y_P is the fraction of Helium in the universe at this redshift and has a value of $Y_P = 1 - X_P = 0.24$.

At each iteration we update the quantity of Q_{H_II} by solving the ODE in equation 36. We solve this ODE by using the 4th order Runge-Kutta numerical algorithm. The details and steps of the numerical scheme are found in Section 3.5.

Once the value of Q_{H_II} is known across the grid we can set the values of the photon destruction probability ε_ν. This is simply a modification to equation 10 since Q_{H_II} can be used to define the opacities of a medium. It is logical that the photon destruction probability depends on the fraction of ionized Hydrogen atoms (due to reasons discussed above). The new definition of ε_ν is found in equation 41 below. This is the definition

that is used in the numerical algorithm.

$$\varepsilon_\nu = \frac{\sigma_\nu(1-Q_{H_{II}})}{\sigma_\nu(1-Q_{H_{II}})+\sigma_T Q_{H_{II}}} \tag{41}$$

σ_T is defined as the Thomson cross section with a value of $\sigma_T = 0.66524587158e-24$ cm^2. σ_{nu} is the photoionization of Hydrogen and is defined as $\sigma_{nu} = 7.91e-18$.
The final variables discussed in Section 3.4 below are updated each iteration and are essential for solving for the new value of the specific intensity.

3.4 Extinction Coefficient and Optical Depth

The extinction coefficient, α, which has units of cm^{-1}, measures how penetrable the medium is. The quantity α is directly correlated with the density, the Hydrogen ion fraction, and a quantum mechanical correction factor for electron energy transitions (known as the Gaunt factor) [31]. Once $Q_{H_{II}}$ has been updated α can be updated using the following formula.

$$\alpha = (1-Q_{H_{II}})\sigma_\nu \rho \tag{42}$$

We then integrate the updated extinction coefficient (equation 42) between two grid points to obtain the change in optical depth (τ) for the respective grid cell. The optical depth is another crucial quantity for tracking RT. Every time the optical depth is updated the Hydrogen gas gets moved around and chemically altered due to the affect and evolution of the radiation between the sources. The following equation is the formal definition of the optical depth.

$$\Delta\tau = \alpha\Delta x \tag{43}$$

Δx is a spatial coordinate usually in units of *cm* and can be converted to any other distance measurement such that it cancels out the units of the extinction coefficient.

When initializing the optical depth we did not use equation 43, but instead used the specified density profile to calculate it. The density field information we used came from the hydrodynamics code CHOLLA [14]. Once the density field was set for each grid point, we used the following equations to calculate the column density of each cell. The column density (μ_ρ) is then used to solve for the optical depth.

$$\mu_\rho = \rho \Delta x \tag{44}$$

$$\Delta\tau = \mu_\rho \sigma_\nu \tag{45}$$

The density in equation 44 has already been converted to comoving units. This was a standard for any relevant variable being used in RT calculation.

The first half of Section 3 has covered all of the physical variables that are used in the numerical computation to solve equation 7. In Section (3.5 and Section 3.6) we describe the algorithm branches that use all of the equations mentioned in order to build the solver desired. These branches include the 4th order Runge-Kutta solver that evolves the Hydrogen ion fraction and solving the source function interpolation for equation 22 to name a couple.

The next section dives into the details of the Runge-Kutta numerical ODE solver.

3.5 Updating the Ionized fraction of Hydrogen Atoms using Runge-Kutta

This section discusses the update of the fraction of Hydrogen ions between the two sources in the astrophysical experiment. We assume that the entirety of the gas is neutral at the start of the simulation. As the iterations evolve, the sources ionize the gas due to the propagation of photons throughout the gas. The equation describing the ioniza-

tion is a constant coefficient, linear, first order, ordinary differential equation (ODE). A general, analytic solution is known for this type of ODE. We chose to use the 4th order Runge-Kutta algorithm to evolve and solve for the value of the Hydrogen ion fraction. In general Runge-Kutta methods are iterative and generate accurate approximate solutions to ODEs. The family of Runge-Kutta methods use both explicit and implicit schemes that vary in precision [32].

For this experiment we use the explicit 4th order Runge-Kutta scheme (known from here as RK4). Explicit methods are less stable than implicit schemes. However, for our experiment we are solving a linear ODE and thus an explicit scheme will perform well.

3.5.1 RK4 Equations

The ODE equation that solves for the ion fraction of Hydrogen can be found in its full form above (equation 36). We can write this same equation in a more condensed form (equation 46).

$$\frac{dQHII}{dt} = f(QHII,\, t),\;\; QHII(0) = 0 \tag{46}$$

Where $QHII$ is the ion fraction and t is time. Equations 47 and 48 define the set of equations, specific to the RK4 method, that produces the numerical approximation to equation 46.

$$\begin{aligned} K_1 &= hf(QHII_n,\, t_n) \\ K_2 &= hf(QHII_n + \frac{h}{2},\, t_n + \frac{K1}{2}) \\ K_3 &= hf(QHII_n + \frac{h}{2},\, t_n + \frac{K2}{2}) \\ K_4 &= hf(QHII_n + h,\, t_n + K3) \end{aligned} \tag{47}$$

$$QHII_{n+1} = QHII_n + \frac{K1}{6} + \frac{K2}{3} + \frac{K3}{3} + \frac{K4}{6} \tag{48}$$

Note that n associated with any variable denotes the previous value of a variable and $n+1$ represents the updated value of the variable. For example, if we are trying to compute the value of $QHII_1$, $(n+1=1)$ the following values are used: $QHII_0 = QHII(t_0)$ where $t_0 = 0$ when $n = 0$.

3.5.2 RK4 Algorithm Steps

Similar to the steps of the ALI and LI schemes Section (3.6) the goal is to solve for the value of the ion fraction at each grid point until convergence is reached. The following steps describe the process in which the RK4 method is integrated into the algorithm.

1. Create a separate subroutine that defines the differential equation being solved. This is equation 36 for our experiment.

2. Take the value of the ion fraction at the current grid cell and plug it into the ODE (equation 36). This produces a value for the rate of change of the ion fraction (and is referred to as the current value of the ODE). Take the current value of the ODE and the ion fraction and plug them into the set of equations listed in equation 47 to solve for each K value.

3. Use the current value of the ODE and all of the K values to solve for the updated $(n+1)$ value of the ODE by plugging them into equation 48.

4. Repeat steps two and three to for each value of the ion fraction across the grid.

This calculation is a key component for tracking the evolution of the effects from radiative transfer and is a critical part of the focus in Section 6. Studying the evolution of the Hydrogen ion fraction with time produces interesting physical insight that cannot be provided by solely tracing the value of the source function or the specific intensity.

3.6 Details of the LI and ALI methods

The LI scheme is a direct, iterative method that takes fewer computational steps per iteration than the ALI algorithm. However the LI method takes more iterations than the ALI method to reach convergence around the correct solution. The LI method struggles in computationally intensive regimes and the method may not converge around the correct solution at all. The instability can also occur if the values of the initial conditions are too large or small from the value of the actual solution. This poses a problem for the situations where the solution is unknown. This would cause extra initial analytic work. These are all challenges that the ALI scheme overcomes.

Certain physical regimes allow the algorithms to perform equally well in terms of accuracy, but the LI scheme is still takes more iterations to reach the solution. However in the situations where the physical regime has a low photon destruction probability (where the LI scheme cannot obtain the solution) the ALI method can rapidly converge around the accurate solution. On the contrary there are also situations where the ALI scheme breaks down due to its own mathematical limits caused by the method used to accelerate the convergence of the source function. In these situations it is necessary to rely on the direct computation of the LI scheme so long as the physical regime is within its computational range. Overall the strengths and weaknesses of these two algorithms are complimentary to each other. This makes it important to have both algorithms available to cover a wider variety of computational problems.

We constructed our code such that it incorporates both the ALI and LI scheme. In Section 4.2-4.4 we discuss and compare the performance of each scheme on certain test problems and confirm that the algorithm is performing correctly before exploring the test problem which is unknown.

3.6.1 The LI scheme

As mentioned above the LI scheme is a straightforward method that only computes the variables required to numerically solve equation 7. There is no external method brought in to accelerate the convergence of one or more of the variables. This is a positive highlight of this method since there are no other computational limitations imposed by any external method. The down side to the LI scheme is that it is slower and has its own computational limit. It cannot handle physically complex computations (e.g. when the photon destruction probability is low). Having this method on-hand within the code is proving to be useful for our cosmological test problem discussed in Section 5.
The following steps describe the numerical LI method.

1. Set the Planck Function across the grid. For our experiment $B_\nu = 1$ for the entire calculation. This can be done at a later step, but this is one of the only variables that did not need to be updated every iteration and thus can be handled first.

2. Initialize the density array of the Hydrogen gas at each grid point. This can be done by iterating through the grid and set each grid cell individually or read in the density profile from an external file. For the astrophysical problem we read in a text file.

3. Compute the column density at each grid cell using equation 44.

4. Compute the change in optical depth for each grid cell using the column density equation 45.

5. Set the interpolation coefficients equations 31, 32, 34, and 35.

6. Set the values of the Hydrogen ion fraction for each grid point by solving equation 36 using RK4 numerical scheme (discussed in Section 3.5). Initially we

set $Q_{H_{II}} = 0$ everywhere for our experiment but then the Hydrogen ion fraction is computed by using the RK4 scheme to iterate until convergence at each grid point.

7. Compute the value of ε_ν across the grid using equation 41. If $Q_{H_{II}} = 0$ then $\varepsilon_\nu = 1$ everywhere.

8. Use the method of short characteristics (equation 30 and equation 33) to find the approximate solution for the specific intensity at each grid point for each of the two rays (I^+ and I^-). If this is the initialization set the values according to specified initial and boundary conditions or read in a text file.

9. Set the values of J_ν across the grid using equation 8. If this is the first iteration and there are no boundary or initial values specified; J_ν can be set to be zero everywhere, or another logical initial guess can be determined.

10. Set the values of the source function using equation 11. Note that if $B_\nu = 1$, $\varepsilon_\nu = 1$, and $J_\nu = 0$ then the source function is $S_\nu = 1$ everywhere.

11. Repeat steps (3) - (10) until S_ν have converged and thus an equilibrium state has been reached.

The next two sections review the details of the steps to the ALI scheme. First we discuss the numerical algorithm that "Accelerates" the convergence around a solution.

3.6.2 The ALI Tridagonal Scheme

We first discuss the accelerated process of the ALI scheme that differentiates it from the LI scheme. The ALI scheme fixes the convergence issue that the LI scheme has. This is done by updating the source function twice each time we update one grid cell compared

to the progression seen in the iterations of the LI scheme. Each scheme updates the source function by using equation 11. Then the ALI scheme uses this updated source term value and passes into a tridiagonal matrix solver that then solves for an even newer source term value. The tridiagonal matrix is built from the interpolation coefficients (equation 31 and equation 34) which depend on the change in optical depth between each grid point. This indicates that the tridiagonal matrix has to be updated every iteration. Even though there are extra numerical steps, the computational run time is reduced. Computational run time is reduced because fewer iterations are required to find convergence around the accurate source function. This acceleration prevents the source term from converging around values that are lesser in value than the actual solution. The details about the tridiagonal matrix are presented in below. This processes follows the lecture notes created by C.P. Dullemond for a graduate course. These notes follow the method presented by Olson, Auer, and Buchler 1986 [33].

In order to accelerate the convergence of the source function additional numerical steps are taken every iteration. Since the source term is dependent on J_ν, we must re-write how we calculate J_ν. J_ν now must be an interpolated value given by equation 49. Recall that the specific intensity values are estimated using the MSC interpolation definitions of the two specific intensity values given by equations 30-35 that are then plugged into equation 8 (the definition of J_ν).

$$\begin{aligned} J_\nu = \frac{1}{2}[&(I^+_{i-\frac{1}{2}} e^{-\Delta\tau_{i-1}} + I^-_{i+\frac{3}{2}} e^{-\Delta\tau_{i+1}}) + \\ &(d^+ \, S_{i-\frac{1}{2}} + d^- \, S_{i+\frac{3}{2}}) + \\ &(p^+ \, S_{i+\frac{1}{2}} + p^- \, S_{i+\frac{1}{2}}) + \\ &(u^+ \, S_{i+\frac{3}{2}} + u^- \, S_{i-\frac{1}{2}})] \end{aligned} \tag{49}$$

The contributions from the source function steer the magnitude of J_ν. This allows us to approximate J_ν to be solely dependent on the values of the source function. The most computationally efficient way to save the interpolated values of J_ν across the grid is by creating a matrix. We then recognize that this matrix is an operator (known from here as the Λ operator) containing the interpolation coefficients. The interpolation coefficients operate on the source function as a vector (representing the values across the 1D grid). The operator definition of J_ν is simply a condensed, linear algebra form of equation 49. If we are to extend our interpolation approximation beyond the third order the matrix operator would no longer be tridiagonal. This causes the accelerated part of the ALI scheme to become more computationally intensive. This more intense method still leads to the rapid convergence of the source term values.

$$J_\nu = \Lambda[S_\nu] \tag{50}$$

The following equations provide the definition of the lower diagonal Λ_a, diagonal Λ_b, and upper diagonal Λ_c components of the Λ operator. If a higher order approximations gets used, the other matrix components are filled in using the interpolation equations.

$$\Lambda_a = \frac{1}{2}(d^+ + d^-) \tag{51}$$

$$\Lambda_b = \frac{1}{2}(p^+ + p^-) \tag{52}$$

$$\Lambda_c = \frac{1}{2}(u^+ + u^-) \tag{53}$$

The operator definition of J_ν, equation 50, can be plugged into equation 11 allowing the source term to be explicitly dependent on the Λ operator (equation 54. This is an explicit relation because equation 11 is by definition solving for the updated value of

the source term at the current grid point. While the Λ operator contains the previous value of the source term at the current grid point. Therefore you can use the 'old' source term value to find the 'new' source term value at the current grid point. However since this is a higher order approximation the neighboring source terms will be taken into account when calculating the newer source term value.

$$S_\nu^{n+1} = \varepsilon_\nu B_\nu + (1-\varepsilon_\nu)\Lambda[S_\nu^n] \tag{54}$$

The updated value of the source function at the current grid point is denoted as S_ν^{n+1} while the old value of the source function at the same grid point S_ν^n.

This explicit equation naturally accelerates the convergence around the correct distribution of the source function. We now make equation 54 implicit, meaning that the source term on the LHS and RHS of the equation is the same value (i.e. $S_\nu = S_\nu$). In order to write the numerical progression of the source term in a more coherent way we re-arrange the implicit form of equation 54 and group the same variables to appear on same on the same side of the equation. This means that all of the terms with S_ν are combined to appear only on the LHS as seen in equation 55.

$$[1-(1-\varepsilon_\nu)\Lambda]S_\nu = \varepsilon_\nu B_\nu \tag{55}$$

We recognize that our only variable is S_ν. Thus the term on the LHS containing Λ can be considered a coefficient matrix called M. To be clear matrix M is defined in equation 56 below.

$$M = [1-(1-\varepsilon_\nu)\Lambda] \tag{56}$$

Plugging in the newly defined coefficient matrix M into equation 54 gives the following equation.

$$MS_\nu = \varepsilon_\nu B_\nu \tag{57}$$

This is a disguised form of the classic matrix equation $Mx = b$. Where the solution to this matrix equation can be written in the following way.

$$S_\nu = \varepsilon_\nu M^{-1} B_\nu \tag{58}$$

It is important to notice the matrix inversion that appears in equation 58. Taking the inverse of a matrix that has a numerical value for each index is complex and computationally expensive even for small matrices. Therefore we need to make some approximations to our matrix in order to solve for the solution using the accelerated method. The first step in making this method computationally feasible is by approximating the full Λ operator with a new operator Λ^*. A type of matrix that allows matrix multiplication, inversion, and storage to be computationally less expensive. However purely diagonal matrices do not approximate the full operator in the most robust way nor does they accurately interpolate the mean specific intensity. They provide a poor set of interpolation equations since neighboring cell values are ignored. The best compromise is to make a tridiagonal approximate operator that satisfies equation 59 and aligns with the third order interpolation scheme. Thus we defined the full Λ operator using the diagonal and tridiagonal operators as follows.

$$\Lambda = (\Lambda - \Lambda^*) + \Lambda^* \tag{59}$$

Plugging equation 59 into the new value of the source function (equation 54) we obtain a definition for matrix M^*.

$$S_\nu = \varepsilon_\nu B_\nu + (1-\varepsilon_\nu)(\Lambda - \Lambda^*)S_\nu + (1-\varepsilon_\nu)\Lambda^* S_\nu \tag{60}$$

$$(1-(1-\varepsilon_\nu)\Lambda^*)S_\nu = \varepsilon_\nu B_\nu + (1-\varepsilon_\nu)(\Lambda - \Lambda^*)S_\nu \tag{61}$$

$$M^* = 1-(1-\varepsilon_\nu)\Lambda^* \tag{62}$$

Re-writing equation 57 using the definition of M^* and differentiating the two source values such that S_ν^{n+1} on the LHS is different than the value of S_ν^n on the RHS gives equation 63.

$$M^* S_\nu^{n+1} = \varepsilon_\nu B_\nu + (1-\varepsilon_\nu)(\Lambda - \Lambda^*)S_\nu^n \tag{63}$$

We then solve equation 63 for S_ν^{n+1} since the goal is to solve for an updated value of the source function at the current grid point.

$$S_\nu^{n+1} = [M^*]^{-1}(\varepsilon_\nu B_\nu + (1-\varepsilon_\nu)(\Lambda - \Lambda^*)S_\nu^n) \tag{64}$$

Finally we expand the multiplication on the RHS of equation 64 and use equation 50 (the operator definition of J_ν) to obtain equation 65. This is the equation that the tridagonal solver uses to accelerate the update of the source term values.

$$S_\nu^{n+1} = [M^*]^{-1}(\varepsilon_\nu B_\nu + (1-\varepsilon_\nu)(J_\nu - \Lambda^* \cdot S_\nu^n)) \tag{65}$$

We will discuss the numerical details about how the tridiagonal matrix algorithm solves equation 65. Although the solver must work through a matrix inversion, the process is computationally feasible for a tridiagonal matrix.

The tridiagonal components of matrix M^* are based on the definitions from Λ^* (equations 66-68). Both matrices are defined by the interpolation coefficients (equation 32 and equation 35). To clarify the Λ^* is the tridiagonal version of Λ thus it can be referred to as the partial Λ operator.

$$\Lambda_a^* = \frac{1}{2}(d^+ + d^-) \tag{66}$$

$$\Lambda_b^* = \frac{1}{2}(p^+ + p^-) \tag{67}$$

$$\Lambda_c^* = \frac{1}{2}(u^+ + u^-) \tag{68}$$

$$M_a^* = -(1-\varepsilon_v)\cdot\Lambda_a^* \tag{69}$$

$$M_b^* = 1-(1-\varepsilon_v)\cdot\Lambda_b^* \tag{70}$$

$$M_c^* = -(1-\varepsilon_v)\cdot\Lambda_c^* \tag{71}$$

The multiplication seen in equation 65 is not a dot product but a component-wise calculation. The value of ε_v and each tridiagonal component Λ_x^* is different for each grid cell.

We incorporate the Thomas algorithm [34] as a subroutine to solve equation 65 efficiently. The Thomas algorithm uses a Gaussian Elimination (GE) and Backward Substitution scheme specifically designed to work with tridiagonal matrices. Since most indices of a tridiagonal matrix are zero it greatly simplifies the GE and Backward Substitution calculation [35]. Writing out the full matrix equation (equation 72) allows us to gain a perspective on how to define the system of equations that need to be solved by

the algorithm.

$$\begin{bmatrix} b_{00} & c_{01} & \dots & \dots & \dots & 0 \\ a_{10} & b_{11} & c_{12} & & & \vdots \\ \vdots & a_{21} & b_{22} & c_{23} & & \vdots \\ \vdots & & \ddots & \ddots & \ddots & \vdots \\ 0 & \dots & \dots & \dots & a_{n-2\ n-1} & b_{n-1\ n-1} \end{bmatrix} \begin{bmatrix} x_0 \\ x_1 \\ \vdots \\ \vdots \\ x_{n-1} \end{bmatrix} = \begin{bmatrix} y_0 \\ y_1 \\ \vdots \\ \vdots \\ y_{n-1} \end{bmatrix} \tag{72}$$

After multiplying each component of the LHS of equation 72 out and setting it equal to the corresponding y-value on the RHS equation we produce equation 73.

$$(a_{i-1,i})\, x_{i-1} + (b_{i,i})\, x_i + (c_{i,i+1})\, x_{i+1} = y_i \tag{73}$$

Equation 73 is the general form of the systems of equations and can be confirmed by [35]. Recall that for the first equation (when $i = 0$) the lower diagonal value $a = 0$. For the final equation (when $i = n$) the upper diagonal component $c = 0$.

Equations 74-77) give the definitions and the steps about how to set the upper diagonal, lower diagonal, and diagonal components of equation 73. By solving for each of these compoents we are actually performing the steps necessary for the forward and backward substitution process for a tridiagonal matrix. The tridiagonal matrix that is plugged into this algorithm is M^*. The reason for this can be seen clearly by comparing equation 57 to the general linear algebra equation $Ax = b$ that is being solved. In equation 57 the vector x is equivalent to the vector S_v^{n+1} (i.e. $x = S_v^{n+1}$).

In order to fully understand the numerical steps we discuss the mathematical notation used. The lower diagonals of the matrix are denoted in a single array called a, the diagonals in b, the upper diagonals in c. The solution array (or the vector of x-values) is denoted as x, and the y-values in y. We are using standard notation such that the ith

value of an array is denoted as $a[i]$. The first value in an array is the set to be 0 and the final value is set to be $n-1$ where n is the size of our grid and *nxn* and the size of the matrix.

1. Define two new arrays, y' and c', and initialize them to be zero everywhere. Then iterate through each element and save each value for the following operation. This is essentially forward substitution.

   For $i = 0$:

$$\begin{aligned} c'[i] &= \frac{c[i]}{b[i]} \\ y'[i] &= \frac{y[i]}{b[i]} \end{aligned} \tag{74}$$

   For $i = 1 : n-2$

$$\begin{aligned} c'[i] &= \frac{c[i]}{b[i] - (a[i] \cdot c'[i-1])} \\ y'[i] &= \frac{y[i] - (a[i] \cdot y'[i-1])}{b[i] - (a[i] \cdot c'[i-1])} \end{aligned} \tag{75}$$

   For $i = n-1$:

$$\begin{aligned} y'[i] &= \frac{y[i] - (a[i] \cdot y'[i-1])}{b[i] - (a[i] \cdot c'[i-1])} \\ x[i] &= y'[i] \end{aligned} \tag{76}$$

2. Once these two new arrays have been set we can then use back substitution to solve for each value in the x array. Note that the $n-1$ value for x has already been set in the previous step.

   For $i = n-2 : 0$

$$x[i] = y'[i] - c'[i] * x[i-1] \tag{77}$$

Notice that the inversion of M^* has a mathematical limit when the denominator in equations 74-77 equal zero. This is the only exposed weak point of this algorithm. However, when M^* cannot be inverted the LI scheme can be applied so long as the environment is within its computational limits.

3.6.3 Steps for the ALI Method

Many of the steps used to carry out the ALI scheme overlap with the LI scheme. Hence why it is convenient for us to include both algorithms in the code.

1. Set the Planck Function across the grid. For our experiment $B_\nu = 1$ for the entire calculation. This can be done at a later step, but this is one of the only variables that did not need to be updated every iteration and thus can be handled first.

2. Initialize the density array of the Hydrogen gas at each grid point. This can be done by iterating through the grid and set each grid cell individually or read in the density profile from an external file. For the astrophysical problem we read in a text file.

3. Compute the column density at each grid cell using equation 44.

4. Compute the change in optical depth for each grid cell using the column density equation 45.

5. Set the interpolation coefficients equations 31, 32, 34, and 35.

6. Set the values of the Hydrogen ion fraction for each grid point by solving equation 36 using RK4 numerical scheme (discussed in Section 3.5). Initially we set $Q_{H_II} = 0$ everywhere for our experiment but then the Hydrogen ion fraction is computed by using the RK4 scheme to iterate until convergence at each grid point.

7. Compute the value of ε_ν across the grid using equation 41. If $Q_{H_{II}} = 0$ then $\varepsilon_\nu = 1$ everywhere.

8. Use the method of short characteristics (equation 30 and equation 33) to find the approximate solution for the specific intensity at each grid point for each of the two rays I^+ and I^-. If this is the initialization set the values according to specified initial and boundary conditions or read in a text file.

9. Set the values of J_ν across the grid using equation 8. If this is the first iteration and there are no boundary or initial values specified; J_ν can be set to be zero everywhere, or another logical initial guess can be determined.

10. Set the values of the source function using equation 11. Note that if $B_\nu = 1$, $\varepsilon_\nu = 1$, and $J_\nu = 0$ then the source function is $S_\nu = 1$ everywhere.

11. Repeat steps (3) - (10) until the solution has converged and thus an equilibrium state has been reached.

12. Compute the lower diagonal, diagonal, and upper diagonal values of M^* by multiplying the current values of the source function with the operator Λ^*.

13. Use the array of source terms (S_ν^n) computed in step (11) and M^* to obtain the updated values of the source function (S_ν^{n+1}) using the tridiagonal solver.

14. Repeat steps (3) - (13) until the solution has converged and thus an equilibrium state has been reached.

4 Test Calculations

4.1 Strömgren Sphere

One of the ways to check the numerical accuracy of the propagation of the Hydrogen ion fraction, calculated by the RK4 algorithm, is by studying the radius of the Strömgren sphere. A Strömgren sphere is the spherical volume of fully ionized Hydrogen atoms around a source of radiation [36]. The brighter the source of radiation is (the greater the photon emission rate), the greater the number of ionized Hydrogen atoms, the greater the radius of the Strömgren sphere. However, the radius of the sphere is not solely dependent on brightness but also on the density of the Hydrogen gas, the temperature, the recombination properties of the atom, and the clumping fraction [36]. The most well known definition of the Strömgren sphere radius is stated by Spitzer in his 1987 book [36]. We use this same definition (equation 78) to guide our calculations.

$$r_{ss} = \frac{3\mathbb{Q}}{4\pi\alpha_B(T)C_{H_II}\langle n_H\rangle} \tag{78}$$

The only new variable introduced is in equation 78 is $\mathbb{Q}$ which is the emission rate of photons from the source. The other constants in equation 78 are defined in Section (3.5) and produce a Strömgren sphere radius in units of *cm*.

As previously mentioned our astrophysical experiment (Section 5) has two sources; a galaxy and the UV background. There is a Strömgren sphere surrounding the galaxy because the galaxy's emission is approximated to appear from a single area. Since the UV background is a continuous source there is no Strömgren sphere surrounding its emission. Based on the chosen redshift of the simulation we can assume certain properties about the galaxy. Specifically we assume what kind of star formation should be occurring in the galaxy and therefore we can estimate the number of photons emitted from

the source. Our initial approximation for the photon emission rate is $\mathbb{Q} = 10^{53.4}\ \frac{photons}{s}$. This value is based on the results from a code produced by [21] and [22]. We also need to approximate the value of the specific intensity for the galaxy. Our initial estimate comes from [37] and is discussed in further detail in Section 5.2.1.

Since the radius of the Strömgren sphere depends on the density profile of the Hydrogen gas we perform a constant density analytical study to estimate the best value for the specific intensity around the massive galaxy. The gas density is the focus of our study because our density profile varies greatly across the grid (since it includes a massive galaxy and IGM gas). Another reason is because equation 78 indicates that the only non-constant variable that the Strömgren sphere depends on is the hydrogen number density $\langle n_H \rangle$. The hydrogen number density depends on the density field as seen in equation 37. Therefore a constant density study allows us to test our algorithm's accuracy on a more simplified problem with a known analytic solution. We also take advantage of this baseline test to try out different grid resolutions to help optimize accuracy and precision.

Using equation 78 we analytically calculate the radius of the Strömgren sphere for nine discrete, constant density profiles for Hydrogen gas. The results from this analytic study are shown in Figure 3.

Figure 3 shows that the Strömgren sphere radius exponentially decays as the thickness of the density field increases. If the constant density field is sparse, the Strömgren sphere radius is extremely sensitive to density variations. This can be seen by examining the large difference between the Strömgren sphere radius at $\rho = 1e-8$ and $\rho = 1e-7$. Once the constant density field becomes large, the increase in magnitude still causes the radius of the Strömgren sphere to decrease but difference between the two radii is less drastic. This can be seen by comparing the value of the Strömgren sphere radius at $\rho = 0.1$ and $\rho = 1.0$. It is important to note that the maximum density

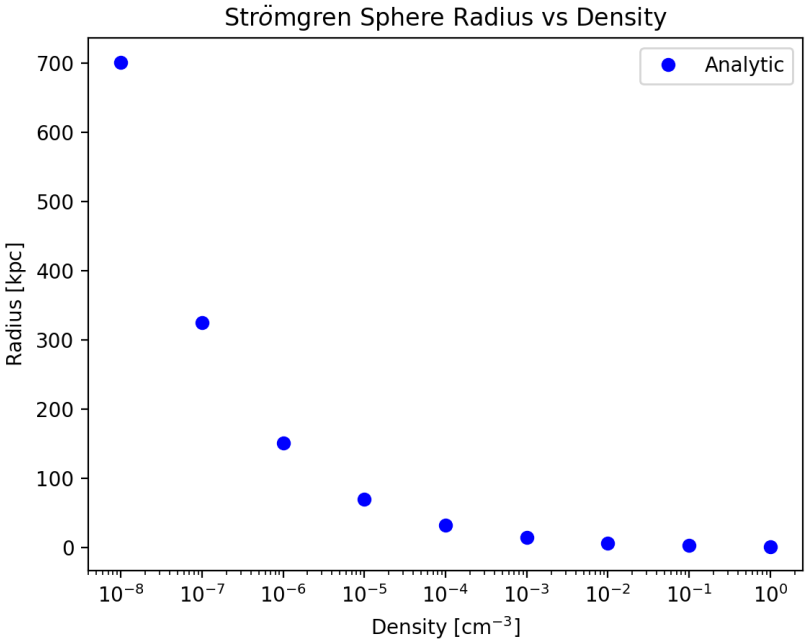

Figure 3: The analytical Strömgren radii for a variation of constant density fields. All of the values shown here are within the range of densities presented by the CHOLLA simulation.

value of our density field, which occurs at the center of the galaxy, is not included in this study. Since the Strömgren sphere radius behaves asymptotically for larger density values we didn't need to probe through the entire spectrum of our density distribution. In the next section we discuss the performance of different grid resolutions and their accuracy in reproducing the analytic Strömgren sphere radius curve seen in Figure 3.

4.1.1 Resolution Study

This study caused us to realize that we needed a finer grid resolution than we had initially predicted in order to capture the physics of our cosmological experiment. Table 2 below shows the minimum distance that can be resolved for each grid resolution. This information helps us determine how accurately a 70 point, 200 point, 500 point, or 1,000 point grid can resolve the analytical Strömgren sphere radius for the given density value. Table 3 shows the density value, the corresponding Strömgren sphere radius, and whether the respective grids could theoretically resolve this radius. If the predicted radius (in kpc) is calculated to be within one grid cell of the analytical value of the Strömgren sphere radius then that density value falls within the capabilities of that grid's resolution. If the distance covered in one grid cell is distinctly greater than the Strömgren sphere radius then the sphere cannot be resolved. This density does not fall within the resolution of that grid because that means the ionization starts and ends inside one grid cell but the physics is not fully captured. Note that none of the grids tested are able to resolve the Strömgren sphere when the density is equal to $\rho = 1e-8$ because the radius of the Strömgren sphere is larger than the total distance of our grid. This defines the lower limit of the density profile for our algorithm. If we were to extend our study further and test higher density values we would also find the maximum limit of the density profile for our algorithm.

As seen in Figure 4 the code rarely produces the correct analytic result for each density

Grid Size	70	200	500	1000
Resolution (kpc per cell)	9.01567	3.12604	1.24666	0.62270

Table 2: Resolution of each grid size

Density ($\frac{1}{cm^3}$)	Analytic $r_{ss}\ kpc$	70 points	200 points	500 points	1000 points
1	1.50987	NR	NR	R	R
0.1	3.25291	NR	R	R	R
1e-2	7.00818	NR	R	R	R
1e-3	15.0987	R	R	R	R
1e-4	32.5291	R	R	R	R
1e-5	70.0818	R	R	R	R
1e-6	150.987	R	R	R	R
1e-7	325.291	R	R	R	R
1e-8	700.818	NR	NR	NR	NR

Table 3: NR = Not Resolved, R = Resolved. Displaying the resolution capabilities of the different grids. The simulation dealt with an entire spectrum of density values and therefore must be able to resolve most of them.

value. Since the variety of resolutions being tested should resolve the Strömgren sphere radius it caused us to realize that we were using the incorrect value for the brightness of the galaxy. One of the other main variables that strongly influences the Strömgren sphere is the photon emission rate which is directly affected by the brightness of the source. This means that the initial value of the specific intensity given by [37] is not correct for our astrophysical experiment. This is acceptable because we are working at a redshift where the brightness of the galaxy and the UV background is disputed over. In Section 5.2.1 we re-do this study where we vary the value of the brightness of the galaxy.

Figure 4 shows that the different grid resolutions do not converge to the analytic solution for most density values. However the grid with 1,000 points provides the finest grid. The finest grid theoretically means that we will be able to resolve density values

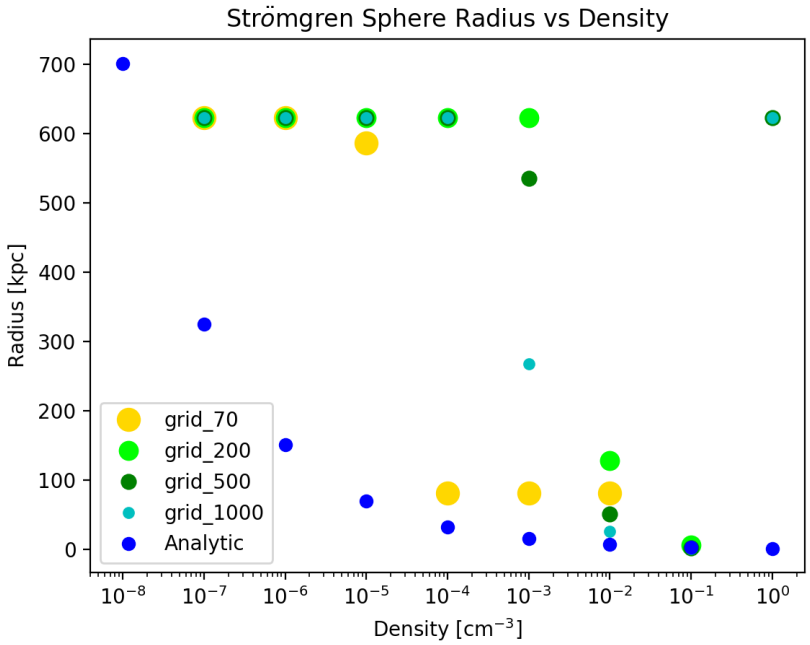

Figure 4: The results of changing the grid resolution when calculating the radius of the Strömgren sphere compared to the actual analytic solution (blue).

that are larger than the ones listed here. However the 1,000 point grid does resolve the maximum density value from the density field produced by CHOLLA. Thus we use the 1,000 point grid for the follow-up Strömgren sphere study in Section 5.2.1 and for the rest of the numerical tests performed in the following sections. These sections test the convergence and accuracy of the ALI and LI schemes to demonstrate the full range of capabilities of the algorithm.

4.2 Two-Stream RT Approximation

The first test case involves a monochromatic atmosphere that only varies in the vertical z direction. This type of problem is known as a plane-parallel atmosphere. This model approximates the radiation at a certain height based on the incoming and outgoing fluxes. This setup has been used to model exoplanet atmospheres [38] and NASA

AMES Mars Climate Modeling Center uses it to model the Martian atmosphere [39]. The details about the atmosphere's density distribution, extinction coefficient (opacity), and photon destruction probability are known. This test experiment is presented in a set of notes given by C.P Dullemond from the Max Planck Institut für Astrophysik (mentioned above).

$$\alpha = 10^{5-6z} \tag{79}$$

$$\Delta\tau_i = \sqrt{3}\alpha_i \Delta z \tag{80}$$

$$\varepsilon = 0.1,\ 0.01,\ 0.001 \tag{81}$$

Here i denotes the current cell where the optical depth is being measured. The $\sqrt{3}$ comes from the angle at which each ray is set: $\mu_+ = \frac{1}{3}$ and $\mu_- = -\frac{1}{3}$. The opacity of the atmosphere is the thickest at the "ground" ($z = 0$) and the thinnest at the "top" ($z = 1$) with exponential decay in between. Finally the photon destruction probability is set to be a constant. Recall that the smaller the opacity is the more scattering occurs which makes for more robust numerical calculations.

A single "source" is set at ground level ($z = 0$) and does not vary with time. We use the time-independent RT equation (equation 7) to propagate the effects of the single, constant source throughout the atmosphere. To show comparative differences in computational intensity we vary the value of the photon destruction probability (equation 81). These different computational regimes emphasize differences between the computational limits of the ALI and LI schemes. Physical regimes where ε is small makes the problem computationally impossible for the LI scheme to converge around. While the ALI scheme can successfully reach convergence around the accurate solution when the photon destruction probability is low. The results for the ALI and LI scheme are compared against each other in Figure 5.

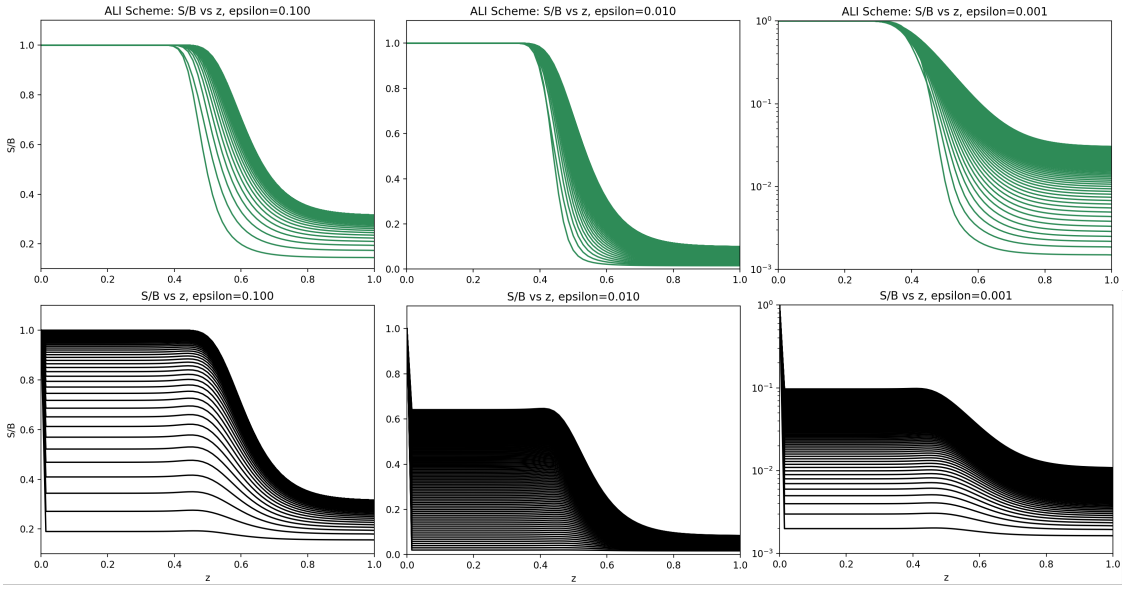

Figure 5: The top (green) panel shows the convergence over 100 iterations of the ALI scheme while the bottom (black) shows the same 100 iterations of the LI method. ε decreases in value from left to right across the atmosphere denoted by z.

It is clear from Figure 5 that as ε decreases the calculation becomes more computationally intensive. The strict LI method (black) is not able to converge to the analytic solution because of this computational difficulty of having a small ε value. This proves the fact that the LI method cannot be blindly trusted. The only environment where the LI scheme is able to obtain the correct solution for the source function over a portion of the grid is when $\varepsilon = 0.1$. Otherwise the LI method shows a large discrepancy between its converged solution and the actual solution to the source function.

While the ALI scheme (green) is able to reach the analytic solution within the same amount of iterations for all three values of ε. It is emphasized that there are limitations to the ALI method since equations 74 - 76 can have a denominator that is equal to zero, in which case the LI method must be used. Therefore the ALI method should also not be blindly trusted.

4.3 Convergence Check

In Section 4.2 the initial specific intensity at the left boundary is set to one (where the source is), and the specific intensity values across the grid are set to zero. This is a simple set of initial conditions which are important to check that the code can reach converges. If these simple test cases do not converge then the more complex initial and boundary conditions will not converge. Due to the implementation of both the ALI and LI schemes our code successfully reached the steady state solution in Section 4.2. The next step to take for testing the abilities of the algorithm is to make the initial conditions more complex. One useful way to do this is by using the final, steady state solution as a set of initial and boundary conditions for another computational run. We will stick to one value of ε for now, but it this ε value will have to be different than the value used in the first computational run which reached the steady-state solution.

The accuracy of the steady-state solution of the second computational run can be determined from runs where the initial state is set simply. This test also exercises the algorithm's ability to read in a set of initial values for the specific intensity. Then use these specific intensity values to correctly compute the mean intensity J and the source function S across the grid (equation 9 and equation 10).

The final trait this convergence test portrays is the algorithm's ability to vary parameters like ε or the optical depth with time. This is an important physical application since we perform an astrophysical setup where the optical depth and the opacity vary over time. Passing this convergence test gives us confidence that our astrophysical application is within the algorithm's capacity.

Figure 6 displays the results of using the final steady-state solution as an initial state before evolving it further under a new value of epsilon. Note how the behavior of the source function at $z = 0$ is the greatest difference between the solution in Figure 6 and

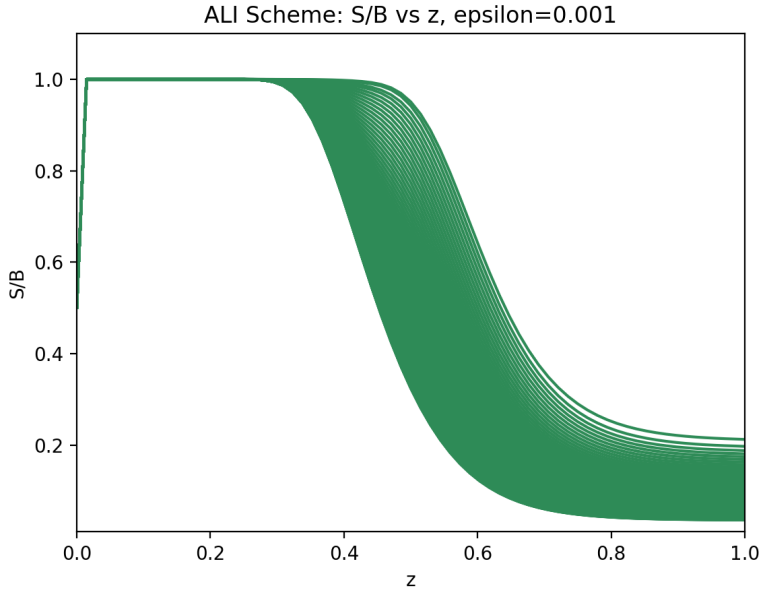

Figure 6: An example where a steady state solution for $\varepsilon = 0.1$ is then used to set the initial state for $\varepsilon = 0.001$ and convergence is achieved.

the solutions shown in Figure 5. Note that the initial boundary conditions for the specific intensity are to be $I^+ = 1 = I^-$, thus making $J = 1$, for all of the experiments performed in Figure 5. In contrast there is no specified initial boundary value for J. J is computed based off of equation 10. Due to the the source function's heavy dependency on the value of J the boundary value for S is also less than one.

Even with the distinct initial boundary value the ALI algorithm converged within 100 iterations to the expected solution. This scheme displays computational ease when computing a solution for $\varepsilon = 0.1$ and $\varepsilon = 0.001$. Having the ability to start in a computationally easy domain and move to a computationally complex regime is a crucial component to solving real world problems.

Up until this point all of the test cases have been run while ε has been held constant. However for the astrophysical experiment ε is spatially variant. It is thus essential to prove that the algorithm can be efficient in this regime too.

4.4 Spatially-varying ε

The last test case, before applying the algorithm to a cosmological setting, involves varying ε across the grid. Briefly mentioned in the previous subsection, the smaller the value of ε the more computationally expensive the calculations per iteration becomes. If $\varepsilon \approx 1$ then a large number of photons, or all of the photons ($\varepsilon = 1$), are annihilated rapidly and thus radiation is not propagated through the medium. On the contrary if $\varepsilon << 1$ then a significant amount of photons propagate through the medium thus making the problem non-trivial. Having a discrepancy between ε at the left and right boundaries is realistic when considering cosmological settings.

For this test case we set the discrepancy of ε between the boundary values to be $\varepsilon << 1$ and $\varepsilon < 1$. This is computationally complex enough to reveal any problems with convergence. The results of the simulation are shown in Figure 7 below.

Figure 7 shows that there are no convergence problems for the ALI scheme when ε is spatially variant. The algorithm is able to reach convergence for the final solution within 100 iterations. This allows us to conclude that there are no problems with the code in this computational regime.

This completes the fundamental test calculations needed to check the accuracy and precision of the algorithm. The next section describes the experimental set up and details of the astrophysical problem.

5 Experiment

5.1 Physical Overview

We investigate the dynamics of RT between a luminous galaxy and the UV background radiation field in the early universe at a redshift of $z = 3$. In between the galaxy and the

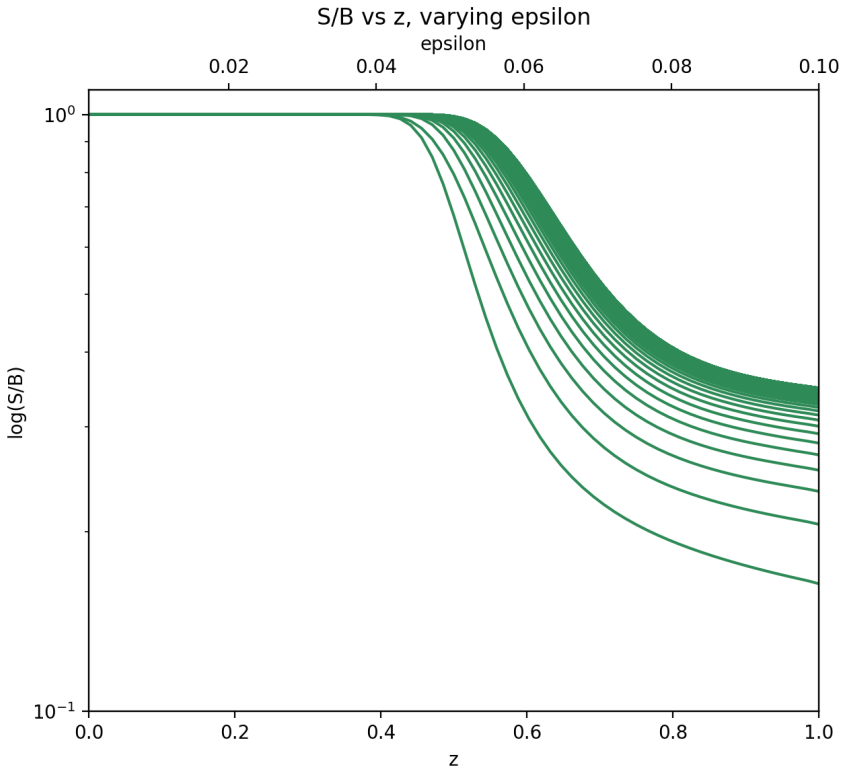

Figure 7: The converged solution where $\varepsilon = 0.001$ at depth $z = 0$ and varied linearly across the grid until reaching $z = 1$ where $\varepsilon = 0.1$.

UV background we assume there is a distribution of gas made of Hydrogen and Helium. The helium gas only absorbs extremely high-energy photons and can be ignored when calculating the absorption. As a percentage of the Hydrogen gas between the galaxy and the UV background become ionized, meaning photons are absorbed and emitted, the specific intensity will also fluctuate. This happens at each time step (equation 7) thus the radiative influence from the galaxy and the UV background also vary every time step until equilibrium is reached. This experiment allows us to further understand the details about how the galaxy and the UV background influence the distribution of ionized Hydrogen atoms in this time period.

We use a third order approximation and the LI scheme to handle the cosmological setting. The reasons why the LI scheme is used over the ALI scheme is discussed in Section 6.1.

5.2 Initial and Boundary Conditions

This experiment required a two-step setup. The first being to set the specific intensity values for our two main sources; the galaxy and UV background. The second is to obtain a steady state specific intensity distribution caused by the interaction of the two sources. The radiation emitted from the galaxy and UV background are handled through two rays (one for each source).

The following go into details about how we initially set the two specific intensity rays for the galaxy and the UV background as well as the density profile of the Hydrogen gas within the galaxy and outside of it.

5.2.1 The Galaxy

The galaxy and the UV background have significantly different specific intensities. We assumed the central galaxy is star-forming. This means it has O and B stars and a certain ratio of binary stars. Rather than spreading these sources throughout the galaxy and treating them individually, we assumed that the majority of the radiation came from the central source. We increased the value of this central source to adjust for these other sources. The brightness of galaxies at this redshift can only be estimated theoretically. Therefore we ended up adjusting the brightness of our galaxy based on the results of the Strömgren sphere radius study. This allowed us to more accurately produce the expected amount of emitted photons.

Since we are treating the galaxy as a large point source, then the brightness throughout the rest of the galaxy must be less than this central value. For our simulation the specific intensity of the center of the galaxy sets our left boundary condition. Recall equation 17 defines the specific intensity based off of the specific luminosity. The specific luminosity falls off with respect to radius as $\frac{1}{radius^2}$. Therefore the specific intensity values across the grid should attenuate in a similar fashion. Figure 8 shows the initial distribution of the normalized and attenuated specific intensity for the galaxy.

For now we disregard the dimensional value of the specific intensity and just use a value of 1 at the center of the galaxy (Figure 8). The rest of the specific intensity values are also dimensionless across are simply attenuated by a factor of $\frac{1}{radius^2}$. Before any dimensional calculation is made the specific intensity is converted back into the appropriate dimensional value. Now that the attenuation of the specific intensity curve is correctly implemented for the galaxy we need to re-visit the Strömgren sphere experiment.

Recall that the specific intensity of the galaxy needs to be adjusted to produce a reason-

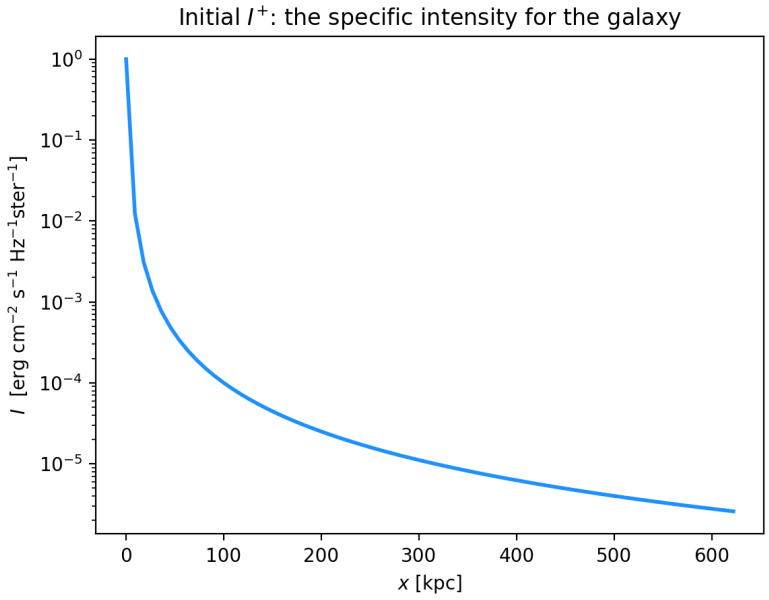

Figure 8: Displaying the $\frac{1}{x^2}$ decay of the specific intensity for a massive galaxy. The center of the galaxy lies at $x = 0$ kpc which is the brightest and main source of the specific intensity. The y-axis is the normalized specific intensity coming just from the galaxy across the grid.

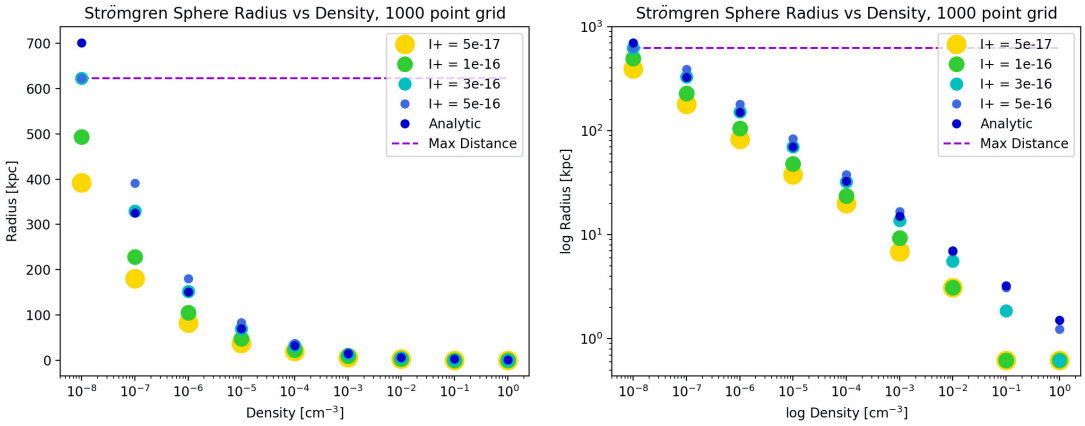

Figure 9: The plot on the left shows how the results from the varying specific intensity values to solve for the radius of the Strömgren sphere compared with the analytic result with only a log scale on the x-axis. The plot on the right shows the log-log version of the plot on the left.

able photon production rate. To our knowledge the code we have written and applied to this environment is unique and therefore we cannot just copy certain aspects of previous computational work. Thanks to [21] and [22] we had a good starting value. Nonetheless in order to match the theoretical Strömgren sphere analytic calculation we needed to deviate from their predictions. We start off by using the given value (from the sources above) for the photon production rate ($Q_0 = 10^5 3.4\ \frac{1}{s}$). This produces a specific intensity value of $I \approx 10^{-17}\ \frac{erg}{sHzcm^2ster}$. When we use this value for the brightness we do not produce a sufficient number of photons to accurately calculate the Strömgren sphere radius for our physical regime. This was confirmed by Figure 3. Thus we incrementally increase the value of the galaxy's brightness until we reproduce a close approximation to the analytical curve within an acceptable range of accuracy. The best value for the specific intensity at the center of the galaxy is $I^+ = 3x10^{-16}\frac{erg}{cm^2\ s\ Hz\ ster}$ as shown in Figure 9.

By changing the value of the specific intensity at the center of the galaxy we are able to more accurately calculate the radius of the Strömgren sphere. This test guides towards

producing a more accurate model of the galaxy with the given gas distribution.

The main criteria used to determine the best value of the specific intensity is to not overestimate the analytical value of the Strömgren sphere radius for each density. This is the case because any overshoot is going to be exaggerated by our algorithm due to the resolution of each grid cell. Therefore it is clear to see from Figure 9 that the value of $I \approx 3e-16\ \frac{erg}{sHzcm^2ster}$ is the closest in value to the analytical solution without overestimating the radius at any density. The photon production rate from the galaxy is thus $Q_0 = 10^5 2.6\ \frac{1}{s}$. This is a reasonable rate because it does not significantly diverge from the values presented the published code produced by ([21] and [22]).

The UV background does not behave like the galaxy. We are viewing the galaxy and UV radiation background from the comoving frame. Meaning that we, the observer, are moving with the expansion of the universe. This makes the universe and background radiation appear isotropic [40]. Thus the UV radiation uniformly radiates rather than falling off as a power law like the galaxy. The details about initializing the UV background can be found in Section 5.2.2 below.

5.2.2 The UV Background

The galaxy is assumed to radiate X-rays or other high frequency light due to the star formation in the gas-rich environment. The light from the galaxy is thus more energetic than the radiation coming from the UV Background. Puchwein et al 2019 [37] found that the UV background has a uniform specific intensity value of $I = 10^{-22}$ $ergcm^{-2}s^{-1}Hz^{-1}rad^{-2}$. This value is calculated based on observations and theoretical results. The specific intensity of the UV background is five orders of magnitude smaller than the center of the galaxy. The specific intensity of the right boundary is set by the UV background. The rest of the specific intensity values across the grid are also set at this constant value. This is the case because the fluctuations in brightness among

the UV background are minuscule and insignificant for the scale and resolution of the simulation.

Now that the two sources and the respective specific intensity rays have been set, the only other component that needs to be determined is the distribution of the hydrogen gas. The gas distribution and composition for a massive galaxy the IGM at a redshift of $z = 3$ is different than the observations made today at $z = 0$. Thus we turn to the output from a cosmological code that studies the evolution of matter and dark matter from an even earlier time period to obtain an accurate distribution of gas for the galaxy and IGM.

5.2.3 Density Field

Bruno Villasenor, a PhD student in the astronomy and astrophysics department at UCSC, has done extensive work on modeling the hydrodynmaics of large scale structure of gas and dark throughout the history of the universe using the open source code called CHOLLA [14]. From one of his three dimensional simulations Bruno is able to extract a one dimensional density skewer through a massive galaxy at $z = 3$. The total distance covered by the skewer is 50 $\frac{Mpc}{h}$. We only used a portion of this skewer and limited it to span 623 kpc. This density information is then read into our code, converted into the desired units, and translated into the comoving frame. The structure from Bruno's simulation does not take into account any affects from radiation so the initial gas density consists of neutral hydrogen. We then center the galaxy on the left boundary of our numerical grid. The density profile throughout our computational domain is shown in Figure 10.

Figure 10 agrees with our physical intuition that the density concentration at the center of a galaxy is several orders of magnitude larger than the gas within the IGM. More specifically the gas within the galaxy is comparable to molecular cloud densities. While

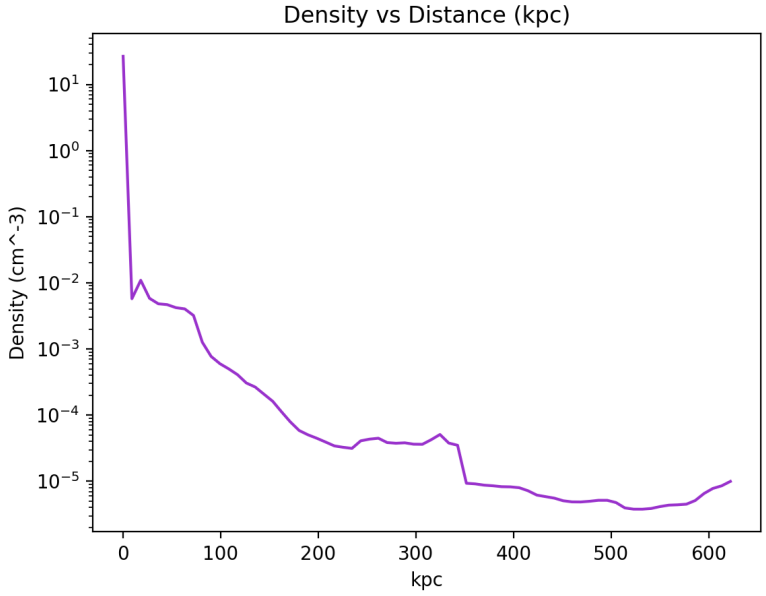

Figure 10: The initial density distribution of Hydrogen gas from the center of the massive galaxy (at $x = 0$ kpc) to the uniform UV background (at $x = 630$ kpc). This distribution came from a snapshot from a hydrodynamic evolution simulation from CHOLLA.

the gas outside of the galaxy is on the atomic cloud density scale.

The extinction coefficient and optical depth (equation 42 and equation 45 respectively) can then be initialized from this density distribution. Once the photons begin to propagate from the two sources, they alter certain portions of the density field. Different parts of the density profile morph at different rates due to uneven density distribution of the gas (Figure 10). This causes inhomogeneous ionization. As inhomogeneous ionization occurs the change in the density distribution causes the extinction coefficient and optical depth to also change making the density a time sensitive variable.

In order to capture the evolving density field on our 1,000 point grid we had to interpolate the given density field. The original density profile from CHOLLA had its own resolution and did not contain 1,000 density points over the desired distance. To perform this interpolation, we use a built in function in Python (Python3 numpy.interp()).

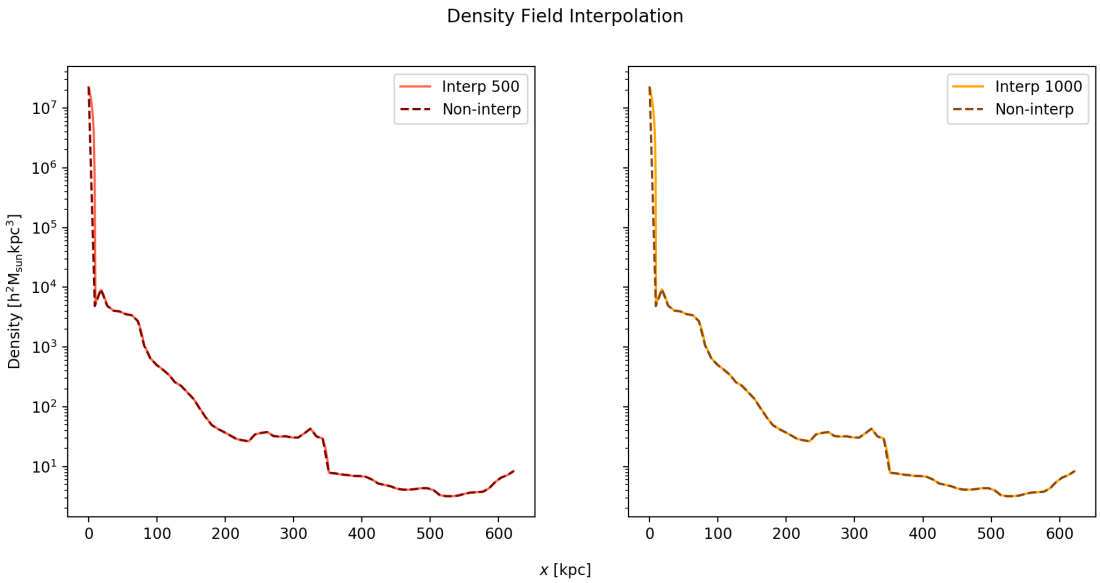

Figure 11: Comparing the interpolation of the density field to the true distribution. The left, red plot shows the comparison for 500 grid points. The left, orange plot shows the resulting field for 1,000 grid points.

Originally the 623 *kpc* density field was defined on 70 grid points. We then tested the accuracy of the interpolation function by examing the detail of the density field for 500 and 1,000 grid points. The results of the density interpolation comparison are shown below in Figure 11.

Figure 11 shows that the built-in interpolation function does a good job whether we are considering hundreds or one thousand of points. There is only a slight deviation from the true density field located at the rapid density decline from the galactic center for both grid resolutions points. The built in function uses a piecewise linear interpolating method. This method connects straight lines between each of the given data points. The linear equations produced by these straight lines are used to estimate the interpolated values [41].

This gives us more confidence in using the 1,000 point grid to better resolve evolution of the ionized Hydrogen atoms, capture the morphology of the density distribution, and

determine the specific intensity to a greater accuracy. The finer grid is more computationally expensive, but this is the necessary to capture the physics of the RT in this astrophysical experiment.

5.3 Reaching a Steady State

There is one last step that must be taken before studying the evolution of radiation from the galaxy and the UV background. The specific intensity throughout the grid must be properly initialized for each radiation source separately. This initialization involves reaching an equilibrium state by evolving each source separately over a long period of time and setting $\varepsilon = 1$ (the photon destruction probability). Due to the initial distribution of the specific intensity the specific intensity can still evolve even if the source function is zero for each grid value (equation 21). According to equation 21 the specific intensity values across the grid will decay at a rate driven by the optical depth at each grid cell.

Figure 12 shows the results of the two computational runs that determine the steady-state specific intensity values for the galaxy and UV background.

As seen in Figure 12 the steady-state distribution of the specific intensity significantly differs from the initial arrangement of the specific intensity values for the galaxy and the UV background (Figure 8 and Section 5.2.2).

For the galaxy the $\frac{1}{x^2}$ specific intensity attenuation effect has been quenched. This makes sense due to the rapid deterioration of the specific intensity values as the distance from the galaxy's central point is increased. The specific intensity decreases rapidly due to the large optical depth values within the galaxy due to the opaque Hydrogen gas.

As for the UV background; the left and right boundaries are held at constant, small spe-

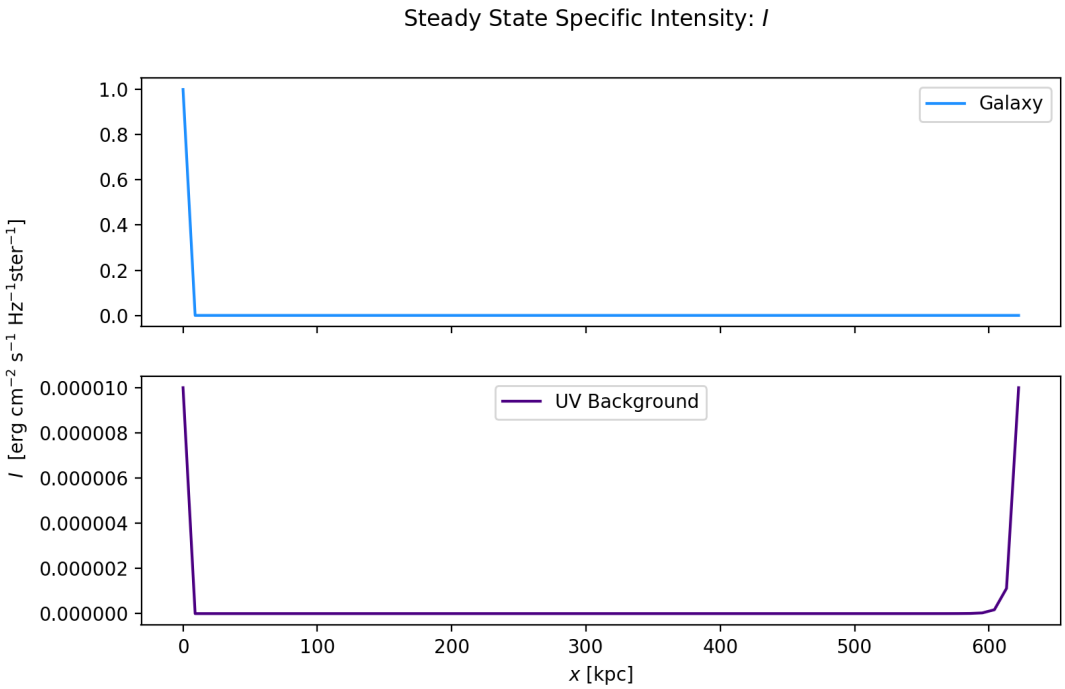

Figure 12: The normalized specific intensity distribution across the grid after a steady state has been reached across the grid between the galaxy and the UV background. The top blue plot shows the normalized specific intensity values from the galaxy. The bottom purple plot shows the values of the normalized specific intensity values from the UV background.

cific intensity values. Due to these small-scale specific intensity values the intermediate specific intensity values will be even closer to zero. This is the case because the UV background is not very bright compared to the galaxy.

Reading in these steady-state specific intensity values as to initial conditions across the grid allows us to set the average specific intensity J_ν. We then set the ion fraction is zero at each grid point, since the gas starts off neutral. The photon destruction probability is calculated based on the ionization state of the gas (equation 41) which means it has a value of one everywhere. This forces the source function to be equal to one everywhere as well (equation 11). This concludes the initialization of all of our variables.

5.4 Escape Fraction

Even though the galaxy and the UV background are treated as independent radiation sources the effects from their radiation on the Hydrogen gas are combined. The galaxy produces hydrogen ionizing photons that propagate through the galactic gas. These photons interact with and ionize the galactic gas, but not all of it. Some of these photons escape the galaxy. The percentage of photons that escape the galaxy and interact with the IGM is known as the escape fraction f_{esc}. The escape fraction is critical to include in cosmological simulations according to [42]. The value of the hydrogen escape fraction has been widely argued to fall within a broad range of values between 1% - 100% [43]; [44]; [45]; [46]; [47].

There are many variables that affect the escape fraction but according to [46] and [30] the mass of the galaxy and the redshift are among the strongest influences. Since we are testing a high mass galaxy at a moderately low redshift value we should use a lower escape fraction value. This comes from knowing that low-mass galaxies at higher redshifts indicate a larger escape fraction value [42].

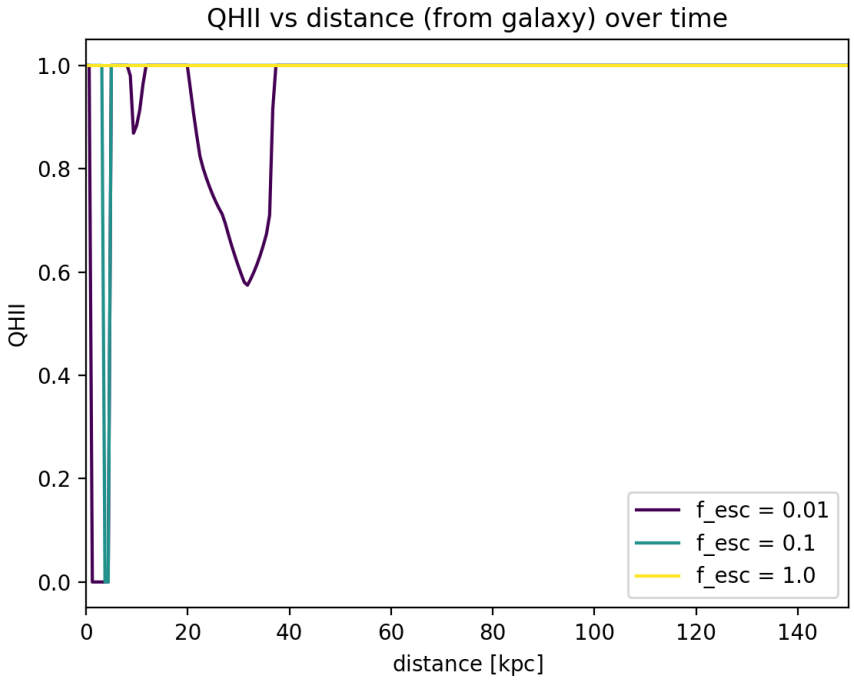

Figure 13: How the hydrogen ion fraction changes when the value of the escape fraction is varied and both the galaxy and UV background are turned on.

At this point we hypothesize that the escape fraction is the main influence for ionizing the gas just outside of the galaxy. Before accounting for the escape fraction we assume that the radiation propagating from the center of the galaxy may not make it all the way through to the edge of the galaxy because of the high density values. The radiation from the UV background may be too dim to influence the gas just outside of the galaxy. Therefore this patch of gas may remain neutral unless the escape fraction is included. There is a dispute over the value of the escape fraction at this redshift. Hence we vary the value of the escape fraction and compare its affects on ionizing the Hydrogen gas just outside of the galaxy. Figure 13 shows these results.

The goal of Figure 13 is to help guide us in picking a value of f_{esc} that ionizes a portion of the gas outside of the galaxy (deemed to be at 100 kpc). However Figure 13 shows

that the gas just outside the galaxy is all ionized regardless of the value of the escape fraction.

This makes us realize that the escape fraction is not going to be the main influence on the ionization of the gas just outside of the galaxy. Figure 13 is showing the result of the galaxy radiating at a specific intensity value of $I^{+} = 3e-16\ \frac{erg}{sHzcm^2ster}$ and the UV background radiating at $I^{-} = 10^{-22}\ \frac{erg}{sHzcm^2ster}$. The galactic source is not bright enough to ionize all of the gas within the galaxy (Figure 13) therefore the galaxy is not responsible for ionizing the outer galactic gas and beyond. Instead the brightness of the UV background is responsible for ionizing all of the gas outside of the galaxy and partially within the galaxy. Based on these results, we maintain a constant escape fraction ($f_{esc} = 0.1$) while varying the UV background's specific intensity value. This should allow us to find the limit at which the UV background is and is not ionizing the entirety of the gas just outside the edge of the galaxy.

6 Test Experiment Results

6.1 ALI vs LI Scheme

We ran the cosmological simulation using both the ALI and LI algorithms. At certain grid cells the change in optical depth is zero. This affects the tridiagonal solver coefficients (equations 74-76) greatly by causing certain calculations to divide by zero. This prevents the ALI scheme from completing the calculation needed to update the source function. This forced us to only use the LI scheme for producing all of the data for the rest of the results. The value of the photon destruction probability did not limit the LI scheme for this experiment.

6.2 UV Background Specific Intensity

The value predicted by Puchwine et al 2019 [37] which is $I^- = 10^{22}\ \frac{erg}{sHzcm^2}$ led to the almost all of the gas within the galaxy and all of the gas in the IGM to be ionized. This ionization occurs because the brightness of the UV background is able to penetrate through the IGM to the outer limits of the galaxy. The outer limits of the galaxy have a lower density and therefore the photons have the ability to continue propagating further into the galactic gas. This caused the UV background radiation to drive the ionization within most of the galactic gas. We vary the brightness of the UV background to find the threshold at which the outer galactic gas region becomes fully ionized. Figure 14 shows the evolution of the different values for I^-.

The transition region where the mean specific intensity is dominated by the galaxy versus the UV background is extremely sensitive to the value of I^- and changes rapidly around $I^- \approx 2.95 \times 10^{-25}\ \frac{erg}{sHzcm^2}$ (Figure 14). If I^- is too intense then the UV background ionizes the intermediate gas and the gas within the galaxy from the outside-in.

For smaller I^- values there is a region in the intermediate density structure, outside the region ionized by the main galaxy, where the gas can become neutral (this region could be referred to as the "outer circumgalactic medium"). Figure 15 shows the transition between the circumgalactic medium when it is neutral to when it is ionized due to the UV background.

The density profile that characterizes the outer circumgalactic medium is shown in Figure 16. This nonlinear density clump is ionized if the UV background is dominating the overall radiation field (i.e. is dominating the mean specific intensity). Otherwise this portion of the density profile remains neutral if the UV background is not dominating the mean specific intensity. This means that the gas on the outer-most edges of the galaxy is more affected by radiation coming from external sources rather than the

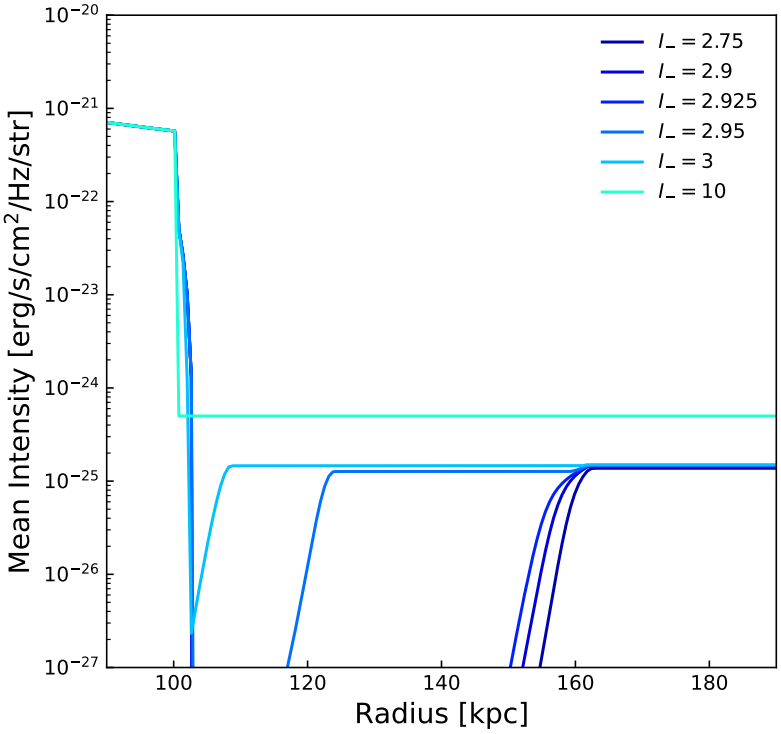

Figure 14: Demonstrating how the mean intensity changes when varying I^- between 10^{-24} and 10^{-25}. The legend is scaled to be read as the following; $10^{-24} = 10$ and $3 \times 10^{-25} = 3$ and so on for all of the values listed.

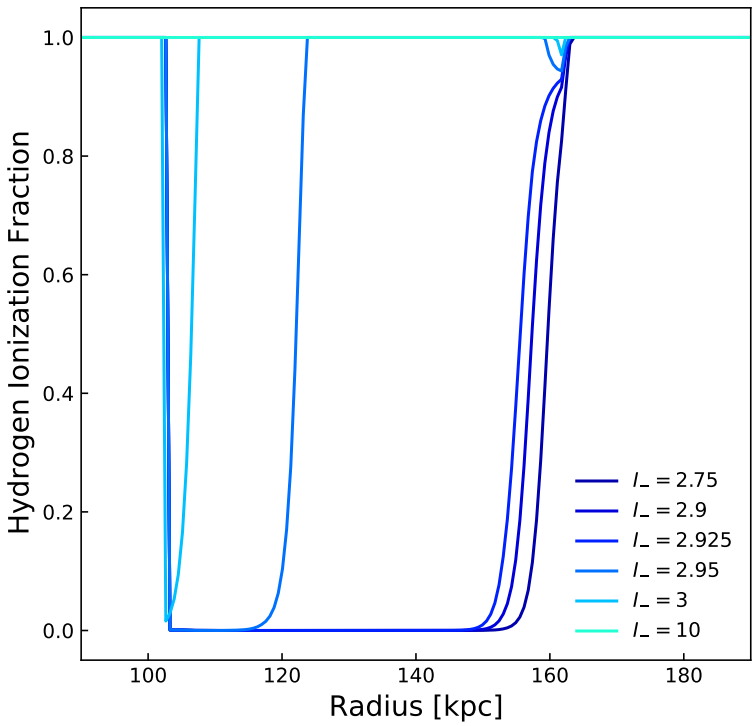

Figure 15: The resulting Hydrogen ion fraction while varying I^- between 10^{-24} and 10^{-25}. The legend is scaled to be read as the following; $10^{-24} = 10$ and $3 \times 10^{-25} = 3$ and so on for all of the values listed.

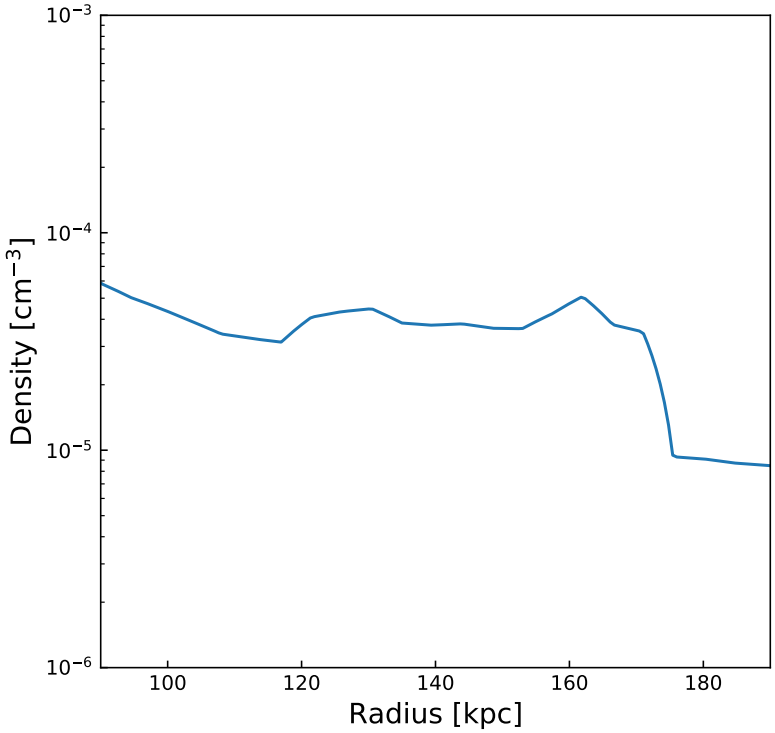

Figure 16: The density profile of hydrogen gas for the outer circumgalactic medium around the galaxy.

internal galactic source.

7 Conclusion

The brightness of the UV background is the main controlling factor in dominating the radiation field responsible for ionizing the galactic gas and the gas within the IGM. This is the case even when the escape fraction is taken into consideration. During the epoch of reionization (which occurs at redshift $z = 7$) the UV background was brighter than the values produced by our results. This could mean that the ionization processes that occurred at that time could have been strongly driven by the brightness of the uniform background radiation.

The algorithm created is successful in terms of accurately calculating an astrophysical problem and various other (smaller) test calculations. The algorithm has the flexibility to use either the LI or ALI scheme. This allows the algorithm to handle a wide variety of problems such as the atmospheric problem presented in Section 4.2 and the cosmological problem in Section 5.

The algorithm also has flexibility in the design to include extra calculations of interest such as the Runge-Kutta ODE solver shown in Section 3.5. This process follows the propagation of the ionization of hydrogen atoms which becomes key when analyzing unknown astrophysical questions. The code also successfully tracks specific the specific intensity values for multiple sources and their combined effects on the test environment.

References

[1] Y.-F. Jiang, J. M. Stone, and S. W. Davis, "A Godunov Method for Multidimensional Radiation Magnetohydrodynamics Based on a Variable Eddington Tensor," *Astrophysical Journals*, vol. 199, p. 14, Mar 2012.

[2] J. Rosdahl and R. Teyssier, "A scheme for radiation pressure and photon diffusion with the M1 closure in RAMSES-RT," *Monthly Notices of the Royal Astronomical Society*, vol. 449, pp. 4380–4403, Jun 2015.

[3] Y. Mao, J. Koda, P. R. Shapiro, I. T. Iliev, G. Mellema, H. Park, K. Ahn, and M. Bianco, "The impact of inhomogeneous subgrid clumping on cosmic reionization," *Monthly Notices of the Royal Astronomical Society*, vol. 491, pp. 1600–1621, Jan 2020.

[4] A. A. Penzias and R. W. Wilson, "A Measurement of Excess Antenna Temperature at 4080 Mc/s.," *Astrophysical Journal*, vol. 142, pp. 419–421, July 1965.

[5] R. H. Dicke, P. J. E. Peebles, P. G. Roll, and D. T. Wilkinson, "Cosmic Black-Body Radiation.," *Astrophysical Journal*, vol. 142, pp. 414–419, July 1965.

[6] S. Dodelson, *Modern cosmology*. 2003.

[7] A. E. Shapley, C. C. Steidel, M. Pettini, and K. L. Adelberger, "Rest-Frame Ultraviolet Spectra of z~3 Lyman Break Galaxies," *Astrophysical Journal*, vol. 588, pp. 65–89, May 2003.

[8] J. Rosdahl, J. Blaizot, D. Aubert, T. Stranex, and R. Teyssier, "ramses-rt: radiation hydrodynamics in the cosmological context," *Monthly Notices of the Royal Astronomical Society*, vol. 436, p. 2188–2231, Oct 2013.

[9] A. Smith, R. Kannan, B. T. H. Tsang, M. Vogelsberger, and R. Pakmor, "Arepo-MCRT: Monte Carlo Radiation Hydrodynamics on a Moving Mesh," *arXiv e-prints*, p. arXiv:2008.01750, Aug. 2020.

[10] D. Aubert and R. Teyssier, "A radiative transfer scheme for cosmological reionization based on a local Eddington tensor," *Monthly Notices of the Royal Astronomical Society*, vol. 387, pp. 295–307, June 2008.

[11] M. Gehmeyr and D. Mihalas, "Adaptive grid radiation hydrodynamics with TITAN," *Physica D Nonlinear Phenomena*, vol. 77, pp. 320–341, Oct. 1994.

[12] M. González, E. Audit, and P. Huynh, "HERACLES: a three-dimensional radiation hydrodynamics code," *Astronomy and Astrophysics*, vol. 464, pp. 429–435, Mar. 2007.

[13] S. M. Kolb, M. Stute, W. Kley, and A. Mignone, "Radiation hydrodynamics integrated in the PLUTO code," *Astronomy and Astrophysics*, vol. 559, p. A80, Nov. 2013.

[14] E. E. Schneider and B. E. Robertson, "CHOLLA: A New Massively Parallel Hydrodynamics Code for Astrophysical Simulation," *Astrophysical Journals*, vol. 217, p. 24, Apr. 2015.

[15] M. Petkova and V. Springel, "An implementation of radiative transfer in the cosmological simulation code GADGET," *Monthly Notices of the Royal Astronomical Society*, vol. 396, pp. 1383–1403, Jul 2009.

[16] J. Mercer, "Sturm-Liouville Series of Normal Functions in the Theory of Integral Equations," *Philosophical Transactions of the Royal Society of London Series A*, vol. 211, pp. 111–198, Jan 1912.

[17] J. Liouville, H. A. Résal, C. Jordan, and H. Villat, "Journal de mathématiques pures et appliquées."

[18] N. Y. Gnedin and J. P. Ostriker, "Reionization of the Universe and the Early Production of Metals," *Astrophysical Journal*, vol. 486, pp. 581–598, Sep 1997.

[19] S. W. Davis, J. M. Stone, and Y.-F. Jiang, "A Radiation Transfer Solver for Athena Using Short Characteristics," *Astrophysical Journals*, vol. 199, p. 9, Mar 2012.

[20] G. B. Rybicki and A. P. Lightman, *Radiative Processes in Astrophysics*. 1986.

[21] J. J. Eldridge and E. R. Stanway, "Spectral population synthesis including massive binaries," *Monthly Notices of the Royal Astronomical Society*, vol. 400, pp. 1019–1028, Dec. 2009.

[22] E. R. Stanway, J. J. Eldridge, and G. D. Becker, "Stellar population effects on the inferred photon density at reionization," *Monthly Notices of the Royal Astronomical Society*, vol. 456, pp. 485–499, Feb. 2016.

[23] B. Hartley and M. Ricotti, "ARC: adaptive ray-tracing with CUDA, a new ray tracing code for parallel GPUs," *Monthly Notices of the Royal Astronomical Society*, vol. 483, pp. 1582–1598, Feb. 2019.

[24] J. P. Bjørgen and J. Leenaarts, "Numerical non-LTE 3D radiative transfer using a multigrid method," *Astronomy and Astrophysics*, vol. 599, p. A118, Mar 2017.

[25] D. Lazzati, "Monte Carlo Radiation Transfer Simulations of Photospheric Emission in Long-duration Gamma-ray Bursts," *Astrophysical Journal*, vol. 829, p. 76, Oct. 2016.

[26] C. P. Dullemond and R. Turolla, "An efficient algorithm for two-dimensional radiative transfer in axisymmetric circumstellar envelopes and disks," *Astronomy and Astrophysics*, vol. 360, pp. 1187–1202, Aug 2000.

[27] P. Kunasz and L. H. Auer, "Short characteristic integration of radiative transfer problems: formal solution in two-dimensional slabs.," *J. Quant. Spectrosc. Radiat. Transfer*, vol. 39, pp. 67–79, Jan 1988.

[28] J. R. Busche and D. J. Hillier, "An Efficient Short Characteristic Solution for the Transfer Equation in Axisymmetric Geometries Using a Spherical Coordinate System," *Astrophysical Journal*, vol. 531, pp. 1071–1080, Mar 2000.

[29] G. L. Olson and P. B. Kunasz, "Short characteristic solution of the non-LTE transfer problem by operator perturbation. I. The one-dimensional planar slab.," *J. Quant. Spectrosc. Radiat. Transfer*, vol. 38, pp. 325–336, Jan. 1987.

[30] J. M. Shull, A. Harness, M. Trenti, and B. D. Smith, "Critical Star Formation Rates for Reionization: Full Reionization Occurs at Redshift z $\approx$ 7," *Astrophysical Journal*, vol. 747, p. 100, Mar. 2012.

[31] A. Burgess and H. P. Summers, "Radiative Gaunt factors," *Monthly Notices of the Royal Astronomical Society*, vol. 226, pp. 257–272, May 1987.

[32] J. C. Butcher, "Numerical methods for ordinary differential equations in the 20th century," *Journal of Computational and Applied Mathematics*, vol. 125, pp. 1–29, Dec. 2000.

[33] G. L. Olson, L. H. Auer, and J. R. Buchler, "A rapidly convergent iterative solution of the non-LTE radiation transfer problem.," *J. Quant. Spectrosc. Radiat. Transfer*, vol. 35, pp. 431–442, June 1986.

[34] A. Povitsky and P. J. Morris, "A Higher-Order Compact Method in Space and Time Based on Parallel Implementation of the Thomas Algorithm," *Journal of Computational Physics*, vol. 161, pp. 182–203, June 2000.

[35] B. N. Datta, *Numerical Linear Algebra and Applications, Second Edition*. USA: Society for Industrial and Applied Mathematics, 2nd ed., 2010.

[36] L. Spitzer, *Physical processes in the interstellar medium*. 1978.

[37] E. Puchwein, F. Haardt, M. G. Haehnelt, and P. Madau, "Consistent modelling of the meta-galactic UV background and the thermal/ionization history of the intergalactic medium," *Monthly Notices of the Royal Astronomical Society*, vol. 485, pp. 47–68, May 2019.

[38] K. Heng, J. M. Mendonça, and J.-M. Lee, "Analytical Models of Exoplanetary Atmospheres. II. Radiative Transfer via the Two-stream Approximation," *Astrophysical Journals*, vol. 215, p. 4, Nov. 2014.

[39] M. A. Kahre, J. L. Hollingsworth, R. M. Haberle, and J. R. Murphy, "Investigations of the variability of dust particle sizes in the martian atmosphere using the NASA Ames General Circulation Model," *Icarus*, vol. 195, pp. 576–597, June 2008.

[40] D. J. Croton, "Damn you, little h! (or, real-world applications of the hubble constant using observed and simulated data)," *Publications of the Astronomical Society of Australia*, vol. 30, 2013.

[41] M. H. Schultz, *Spline analysis*. Englewood Cliffs, N.J. : Prentice-Hall, 1972. Chapter bibliographies.

[42] A. Benson, A. Venkatesan, and J. M. Shull, "The Escape Fraction of Ionizing Radiation from Galaxies," *Astrophysical Journal*, vol. 770, p. 76, June 2013.

[43] J. B. Dove, J. M. Shull, and P. R. Maloney, "What Are The Ionization Sources Of The Diffuse Ionized Medium?," in *American Astronomical Society Meeting Abstracts*, vol. 197 of *American Astronomical Society Meeting Abstracts*, p. 42.11, Dec. 2000.

[44] K. Wood and A. Loeb, "Escape of Ionizing Radiation from High-Redshift Galaxies," *Astrophysical Journal*, vol. 545, pp. 86–99, Dec. 2000.

[45] M. Ricotti, N. Y. Gnedin, and J. M. Shull, "The Fate of the First Galaxies. II. Effects of Radiative Feedback," *Astrophysical Journal*, vol. 575, pp. 49–67, Aug. 2002.

[46] N. Y. Gnedin, A. V. Kravtsov, and H.-W. Chen, "Escape of Ionizing Radiation from High-Redshift Galaxies," *Astrophysical Journal*, vol. 672, pp. 765–775, Jan. 2008.

[47] H. Yajima, J.-H. Choi, and K. Nagamine, "Escape fraction of ionizing photons from high-redshift galaxies in cosmological SPH simulations," *Monthly Notices of the Royal Astronomical Society*, vol. 412, pp. 411–422, Mar. 2011.